CIRRUS PARTICLE SIZE DISTRIBUTION BIMODALITY DERIVED FROM GROUND-BASED RADAR-LIDAR RETRIEVALS

by

Yang Zhao

A thesis submitted to the faculty of
The University of Utah
in partial fulfillment of the requirements for the degree of

Master of Science

Department of Atmospheric Sciences

The University of Utah

May 2011

The University of Utah Graduate School

STATEMENT OF THESIS APPROVAL

The thesis of _____

has been approved by the following supervisory committee members:

_____ , Chair _____
Date Approved

_____ , Member _____
Date Approved

_____ , Member _____
Date Approved

and by _____ , Chair of

the Department of _____

and by Charles A. Wight, Dean of The Graduate School.

ABSTRACT

To better understand the role of small particles in the microphysical processes and the radiative properties of cirrus, the reliability of the historical in situ measurement database must be understood. A means of establishing this validity is to assume that the in situ measurements are at least consistent, in a broad sense, with the remote sensing data, and vice versa. In this study, an algorithm using Doppler radar moments and Raman lidar extinction is developed to retrieve a bimodal particle size distribution and its uncertainty. Case studies and statistics compiled over an entire year show that the existence of high concentrations in excess of 1 cm^{-3} of small particles in cirrus is not consistent with any reasonable interpretation of remote sensing data and is therefore likely from an artifact of the in situ measurement process. This study shows that while the particle concentrations from the Two-Dimensional Cloud Probe generally agree well with the retrieval results, simultaneous concentrations from the Forward Scattering Spectrometer Probe are much higher than the concentrations of small particles implied by the remote sensing measurements. The one-year statistics of the cirrus microphysical properties, including the ice water content, the effective radius and the total particle concentration, show that the occurrence frequency of the concentrations larger than 1 cm^{-3} is below 1%, and, given the possibility of errors in retrieved concentration as large as 100%, this study concludes that the existence of particle concentrations in cirrus in excess of 1 cm^{-3} is extraordinarily rare instead of common as suggested by uncritical acceptance of in situ data.

TABLE OF CONTENTS

LIST OF FIGURES

LIST OF TABLES

CHAPTER 1

INTRODUCTION

1.1 Motivation

Cirrus clouds play an important role in regulating the earth's energy budget through their interactions with the solar and terrestrial radiation. However, they remain a poorly understood component of the climate system (Stephens, 2005). To better represent the feedback of cirrus on the climate system in global climate models, the processes that control the evolution of the macrophysical and microphysical properties of cirrus must be understood as well. This chain of understanding must rest on a foundation of reliable measurements of microphysical properties, including particle size distributions (PSD) and integral properties of the PSD such as water content, mean particle size, and total particle concentration.

At the microphysical level, how light is scattered by ice crystals, especially small ice crystals, is critically important to the solar radiative properties of cirrus, which have a large impact on the albedo of the earth. Heymsfield and Platt (1984) found that as much as 53% of the total visible extinction could be due to small particles in the size range of 1-20 microns. Arnott et al. (1994) showed that small particles could contribute significantly to and sometimes dominate both the solar extinction and the infrared emission. So to better quantify the scattering effects of ice crystals, many field experiments have been conducted and many in situ measurements have been made. For

example, based on in situ measurements from the Forward Scattering Spectrometer Probe (FSSP) and the laser imaging Two-Dimensional Cloud Probe (2DC) from 17 flights in midlatitude cirrus during the Atmospheric Radiation Measurement (ARM) and First International Satellite Cloud Climatology Project (ISCCP) Regional Experiment (FIRE) Intensive Observation Periods (IOP), Ivanova et al. (2001) parameterize cirrus Particle Size Distribution (PSD) as bimodal, one mode for small particles and the other mode for large particles. Gayet et al. (2002) show that high concentrations (5 to 10 cm^{-3}) of small ice crystals are a relatively common microphysical feature of cirrus clouds by using combined measurements from four different in situ instruments: the Counterflow Virtual Impactor (CVI), the Polar Nephelometer, the FSSP and the 2DC during the Interhemispheric Differences in Cirrus Properties From Anthropogenic Emissions (INCA) field experiment. Based on 22 Learjet missions flown in midlatitude cirrus, Lawson et al. (2006) conclude that small particles with maximum dimension less than 50 microns account for 99% of the total number concentrations, 69% of the extinction, and 40% of the mass in midlatitude cirrus.

However, recent studies also suggest that some in situ measurements, such as measurements from the FSSP, may be contaminated by ice crystal shattering on probe inlets, and the particle shattering may have a big effect on the in situ measurements. For example, Field et al. (2003) show that the ice particle interarrival times measured by a fast FSSP can be well characterized by a Markov chain model with two independent Poisson processes, and the debris from ice crystal shattering and the unaffected particles may be the sources for these two different Poisson processes. Korolev and Isaac (2005) demonstrate two possible physical mechanisms for the ice crystal shattering: mechanical

impact with the probe arms and interaction with the aerodynamic field around the probe housing. By using data from Optical Array Probes (OAP) 2DC, OAP 2DP and the high volume precipitation spectrometer, they found that the fraction of shattered ice crystals may make up more than 10% of the total number of sampled particles for aggregates of dendrites. Heymsfield (2007) further investigated the shattering effects on measurements from the Cloud and Aerosol Spectrometer (CAS), the Cloud Integrating Nephelometer (CIN), as well as the FSSP, and he suggests that shattering adds about 15% to the large IWC from the FSSP, and the shattering effect on FSSP and CIN measurements is even more for optical extinction. By using the in situ measurements from the Tropical Warm Pool International Cloud Experiment (TWP-ICE), McFarquhar et al. (2007) showed that the number concentrations of particles with $3 < D < 50$ microns (D: maximum dimension) measured by the CAS with an inlet are 91 (with standard deviation of 127) times larger than those from the Cloud Droplet Probe (CDP), which does not have an inlet, and thus has no effect from the inlet shattering.

Some researchers recently use satellite retrievals to compare with airborne in situ measurements, and provide indirect evidence of the particle shattering effect. For example, Davis et al. (2009) show that the ratio of optical thickness to effective diameter from the in situ measurements differs from the MODIS value in a manner that is roughly consistent with previous claims of the particle shattering effect. However, they also claim that biases in the MODIS retrievals cannot be ruled out.

In this study, to further verify the airborne in situ measurements of small particles in cirrus, the number concentration measurements from the FSSP will be directly compared to the ground-based remote sensing retrievals. Measurements from two active remote

sensors, millimeter wavelength Doppler radar and Raman lidar, will be used in the retrieval algorithm, and an inversion technique will provide both the optimal solutions for retrievals and the retrieval uncertainties.

1.2 Data and Method Overview

The remote sensing measurements used in this study are from the Millimeter Wavelength Cloud Radar (MMCR) and the Raman lidar at the ARM Southern Great Plain (SGP) site.

The ARM MMCR radars are zenith-pointing radars that operate at a frequency of 34.86 GHz. The calibration uncertainty for the radar reflectivity is about 1-2 dBZ, and the uncertainty for the mean Doppler velocity and spectral width is about 0.1 m s^{-1} (Clothiaux et al., 1999). The MMCR radar data used in this study are the water-equivalent radar reflectivity factor Z_e, and the cloud particle terminal fall velocity V_{dq}, which is retrieved from an algorithm described in Deng and Mace 2006 (hereafter DM06).

The ARM Raman lidar is currently operational only at the SGP site, and the lidar data used in this study are the extinction estimated from the lidar measurements (Goldsmith et al., 1998). For Raman lidar, the inelastic (Raman) backscatter signal is affected only by extinction, so the formalism used to estimate the optical extinction does not suffer from the fact that two physical quantities, the aerosol backscatter and extinction coefficients, must be determined from only one measured lidar signal, which is the case for lidar systems built based on elastic scattering (Ansmann et al., 1990). The details of the formalism to derive extinction from Raman lidar measurements can be found in Ansmann et al. (1990) and the calculations were performed by Dr. Jennifer Comstock of the Pacific

Northwest National Laboratory (Comstock, personal communication, 2007).

In sum, the remote sensing data used in the algorithm are the radar reflectivity factor from the MMCR, the terminal fall velocity retrieval from the algorithm described in DM06, and the lidar extinction estimated from Raman lidar measurements.

The approach used to address the question of the concentrations of small particles is first to assume that the PSD is bimodal, as suggested by the in situ measurements. Then, since lidar measurements are sensitive to small particles in cirrus while radar measurements are more sensitive to large particles, lidar and radar measurements are used to calculate the first guesses of small mode PSD parameters and large mode PSD parameters, respectively. Specifically, two modified gamma functions are used to approximate these two modes, and then based on forward model equations from radar reflectivity, Doppler velocity and lidar extinction. An inversion of the forward model equations is based on a Maximum A Posteriori (MAP) criterion, and a Gaussian PDF assumption is used to get both the optimal estimates of the PSD parameters and their retrieval uncertainties. The PSD retrievals from the remote sensing measurements are compared with the PSD in situ measurements to test consistency. Finally, the statistics of the microphysical properties from one year of retrievals is examined to see if the remote sensing data are consistent with the ubiquitous occurrence of high concentrations of small particles in cirrus.

The details of the retrieval algorithm are described in Chapter 2, and a case study is performed in Chapter 3 using the data from the 2000 Cloud IOP. In Chapter 4, long-term observations at the ARM SGP site are used to give the statistics of cirrus microphysical properties, and a summary is given in Chapter 5.

CHAPTER 2

ALGORITHM DEVELOPMENT

2.1 Particle Size Distribution Assumption

We allow for the possibility that the particle size distribution (PSD) of a cirrus volume could have distinct populations of small and large particles that may be entirely unrelated to one another. This allowance requires a bimodal size distribution assumption in the retrieval algorithm.

The bimodal size distribution assumption has been used in previous applications such as in cirrus cloud models (Mitchell, 1996) and also in the parameterization of visible extinction for ice clouds (Platt et al., 1997). Donovan (2003) was the first to use the bimodal size distribution assumption in a retrieval algorithm to estimate ice cloud effective particle size profiles. In his algorithm, two generalized gamma functions with three parameters fixed to constants are used to represent the particle size distribution. In the algorithm developed here, two modified gamma functions are used to approximate the small particle mode and the large particle mode separately, and for each mode the gamma function has the following form:

$$N_x(D) = A_x\left(\frac{D}{D_{g,x}}\right)^{\alpha_x} \exp\left(\frac{D - D_{g,x}}{D_{g,x}}\right) \tag{2.1}$$

where subscript x stands for the large particle mode (l) and the small particle mode (s), D is the particle maximum dimension, $D_{g,x}$ is the distribution parameter that controls the slope of the distribution, A_x is the number of particles per unit volume per unit length at the size $D_{g,x}$, and α_x is the parameter to control the breadth of the distribution.

Subscript l and s are used to stand for the large mode and small mode parameters, respectively, of the bimodal particle size distribution. So the bimodal PSD $N(D)$ can be expressed as:

$$N(D) = N_l(D) + N_s(D) \tag{2.2}$$

This distribution, in its most general form, has six independent degrees of freedom. One example distribution is shown in Figure 1.

2.2 Forward Model

The algorithm is formulated in terms of three measurables: the liquid water equivalent radar reflectivity factor (Z_e), the Doppler velocity (V_d) observed at a wavelength that is large with respect to D, and the extinction (β_{ext}) derived at a wavelength that is small with respect to D. Z_e provides information that is strongly weighted to the largest particles in $N(D)$, and when a prominent large particle mode is present, can be nearly entirely determined by it. β_{ext} is determined by the second moment of $N(D)$ and, when a prominent small mode is present, this quantity can be nearly entirely described by the small mode PSD. V_d, on the other hand, provides a bridge between the large and small particle modes since the particle terminal velocity depends on the ratio of the particle

mass to cross sectional area (Mitchell, 1996) although the V_d measurement is weighted by Z_e and, therefore, has a similar large particle weighting.

In the following development, the forward model equations describing the measured quantities are derived in terms of the assumed bimodal particle size distribution. It should be noted that the derivation of the forward model equations depends on assumptions regarding the distribution of certain intensive properties such as mass and cross sectional area as a function of particle maximum dimension. These relationships depend on the assumed ice crystal habit. The resulting uncertainties due to these assumptions are discussed in detail.

2.2.1 Radar Reflectivity

Since Rayleigh scattering is valid for particles less than 800 microns at 35 GHz wavelength (Donovan et al., 2004), under the assumption of Rayleigh scattering, and assuming for the moment that the cloud particles are solid spheres, the radar reflectivity factor *Z* can be written as:

$$Z = \int_0^\infty N(D) D^6 dD \tag{2.3}$$

However, for cirrus clouds, the ice crystals are not spherical, so it is common practice to use water-equivalent radar reflectivity factor Z_e instead of *Z*, and it can be expressed as:

$$Z_e = \int_0^\infty a_z N(D) D^{b_z+6} dD \tag{2.4}$$

where parameters a_z and b_z are power law parameters to fit the radar backscattering cross section from ice crystals with a certain shape (Aydin et al., 1999).

Following DM06, the power law parameters a_z and b_z can be expressed in terms of the coefficient a_m and exponent b_m in a mass-dimensional power law relationship $M(D) = a_m D^{b_m}$ as:

$$a_z = \left| \frac{K_i}{K_w} \right|^2 \left(\frac{6}{\pi \rho_i} \right)^2 a_m{}^2 \tag{2.5}$$

$$b_z = 2b_m - 6 \tag{2.6}$$

where ρ_i is the density of solid ice, K_i is the complex dielectric factor for ice and K_w is the complex dielectric factor for water.

Substituting Equation (2.2) into Equation (2.4), and integrating over all particle sizes, Z_e can be expressed as a function of size distribution parameters and radar backscattering cross section parameters a_z and b_z:

$$Z_e = \sum_{x=l,s} Z_{e,x} = \sum_{x=l,s} A_x e a_{z,x} D_{g,x}^{b_{z,x}+7} \Gamma\left(\alpha_x + b_{z,x} + 7\right) \tag{2.7}$$

where Γ stands for a gamma function.

2.2.2 Doppler Velocity

The full Doppler spectrum measured by Doppler radar can be described as the convolution of a quiet-air Doppler spectrum that depends on *N(D)* with a probability density function of turbulence (e.g., Gossard, 1994) that is superimposed on a mean updraft or downdraft of speed w_{air}. Deng and Mace applied a deconvolution technique to retrieve the particle terminal velocity in quiet air, V_{dq}, using the first three moments of the radar Doppler spectrum (DM06). Based on their retrievals, we take $V_{dq} = V_d - w_{air}$ and write:

$$V_{dq} = \frac{1}{Z_e}\int_0^\infty V(D) a_z N(D) D^{b_z+6} dD \tag{2.8}$$

where $V(D)$, the fall speed of an ice crystal of maximum dimension D, is parameterized by a power-law expression as:

$$V(D) = a_v D^{b_v} \tag{2.9}$$

Using the coefficients of Mitchell (1996) and the development of DM06, the empirical coefficient a_v and exponent b_v depend on the particle habit assumptions and the air density:

$$a_v = a\nu\left(\frac{2a_m g}{\rho_a \nu^2 a_a}\right)^b \tag{2.10}$$

$$b_v = b(b_m + 2 - b_a) - 1 \tag{2.11}$$

where ν is the kinematic viscosity, ρ_a is the air density, a_a and b_a are coefficient and exponent of an area-dimensional power law relationship, and a, b are coefficient and exponent of a Reynolds number-Best number power law relationship.

Substituting Equation (2.2) into Equation (2.8) and integrating over all particle sizes, V_{dq} can be expressed analytically as:

$$V_{dq} = \sum_{x=l,s} V_{dq,x} = \sum_{x=l,s} a_{v,x} D_{g,x}^{\,b_{v,x}} \frac{\Gamma(\alpha_x + b_{z,x} + b_{v,x} + 7)}{\Gamma(\alpha_x + b_{z,x} + 7)} \tag{2.12}$$

So once the coefficient a_v and exponent b_v are calculated according to Equation (2.10) and Equation (2.11), V_{dq} can be expressed as a function of the size distribution parameters only.

2.2.3 Optical Extinction

The extinction coefficient can be expressed as a function of particle size distribution:

$$\beta_{ext} = \int_0^\infty Q_{ext}(D) A(D) N(D) dD \tag{2.13}$$

where Q_{ext} is the extinction efficiency, and $A(D)$ is the cross sectional area of a particle of size D.

In this study, β_{ext} is derived from Raman lidar measurements using the formalism provided by Ansman et al. (1990). Since the wavelength of the Raman lidar at the ARM SGP site (387 nm) is tens to thousands of times smaller than cirrus particle sizes, the size parameter $x = \frac{2\pi r}{\lambda}$ falls in the geometric-optics regime, so the extinction efficiency Q_{ext} can be approximated as a constant 2. Following Mitchell (1996), $A(D)$ can be expressed by empirical parameters a_a and b_a as:

$$A(D) = a_a D^{b_a} \tag{2.14}$$

Substituting Equation (2.2) and (2.14) to Equation (2.13), and integrating over all sizes, results in:

$$\beta_{ext} = \sum_{x=l,x} \beta_{ext,x} = \sum_{x=l,x} 2A_x e a_{a,x} D_{g,x}{}^{b_{a,x}+1} \Gamma(\alpha_x + b_{a,x} + 1) \tag{2.15}$$

2.2.4 Parameter Reduction and the Fourth Forward Model Equation

So far, three measurements from radar and lidar are used to constitute three forward model equations. However, the assumed $N(D)$ has six free parameters. To solve this severely underdetermined problem, the size distribution parameters are simplified by assuming two free parameters and a fourth forward model equation that is derived based on an assumed relationship between the two PSD modes.

As discussed in section 2.1, each size distribution mode has three independent

parameters: A_x, $D_{g,x}$, and α_x. Parameter α_x affects the breadth of the distribution, and since two modes are used to represent the size distribution, the breadth of the distribution can be effectively changed by adjusting the slope of the large mode. So parameter α is the least important parameter in the algorithm and it is hereafter fixed to an integer value of one for both the small mode and the large mode.

To derive a fourth forward model equation, it is reasonable to say that at some size (D_q), the concentrations of $N_x(D)$ must be the same, or, in other words, the ratio of the number concentrations of these two modes at D_q should be unity, and a fourth forward model equation is expressed as:

$$R = \frac{N_s(D_q)}{N_l(D_q)} = 1 \tag{2.16}$$

In Equation (2.16), D_q is unknown, so in the algorithm, D_q is iteratively adjusted within a specified range, solving the system of equations using optimal estimation to find a value of D_q that best fits the radar and lidar measurements.

In sum, four forward model equations in an analytical form are as follows:

$$Z_e = \sum_{x=l,s} Z_{e,x} = \sum_{x=l,s} A_x e a_{z,x} D_{g,x}^{\,b_{z,x}+7} \Gamma(\alpha_x + b_{z,x} + 7) \tag{2.17}$$

$$V_{dq} = \sum_{x=l,s} V_{dq,x} = \sum_{x=l,x} a_{v,x} D_{g,x}^{\,b_{v,x}} \frac{\Gamma(\alpha_x + b_{z,x} + b_{v,x} + 7)}{\Gamma(\alpha_x + b_{z,x} + 7)} \tag{2.18}$$

$$\beta_{ext} = \sum_{x=l,s} \beta_{ext,x} = \sum_{x=l,s} 2A_x e a_{a,x} D_{g,x}^{\,b_{a,x}+1} \Gamma(\alpha_x + b_{a,x} + 1) \tag{2.19}$$

$$R = \frac{A_s (\frac{D_q}{D_{gs}})^{\alpha_s} \exp(-\frac{D_q - D_{gs}}{D_{gs}})}{A_l (\frac{D_q}{D_{gl}})^{\alpha_l} \exp(-\frac{D_q - D_{gl}}{D_{gl}})} = 1 \tag{2.20}$$

2.2.5 Expressions for the Microphysical Properties

Once the particle size distribution is retrieved, the cirrus microphysical properties such as ice water content (IWC), mass-weighted mean particle size (D_m), and number concentration of total particles (N_t) can be derived from the particle size distribution parameters. Using a mass-dimensional power law relationship as before, and integrating over all particle sizes, the IWC can be written as:

$$IWC = \int_0^\infty a_m D^{b_m} N(D) dD = \sum_{x=l,s} A_x a_{m,x} e D_{g,x}^{\,b_{m,x}+1} \Gamma(b_{m,x} + \alpha_x + 1) \tag{2.21}$$

Similarly, D_m can be expressed as:

$$D_m = \frac{\int_0^\infty a_m D^{b_m+1} N(D) dD}{\int_0^\infty a_m D^{b_m} N(D) dD} = \sum_{x=l,s} D_{g,x} \frac{\Gamma(\alpha_x + b_{m,x} + 2)}{\Gamma(\alpha_x + b_{m,x} + 1)} \tag{2.22}$$

N_t becomes:

$$N_t = \int_0^{\infty} N(D)dD = \sum_{x=l,x} A_x e D_{g,x} \Gamma(\alpha_x + 1) \tag{2.23}$$

2.3 Retrieval Algorithm Implementation

From the discussion of the forward model equations, we can see that the radar and lidar measurements can be described using four PSD parameters that are to be retrieved using twelve empirically specified parameters in four forward model equations. If using vector $\mathbf{d} = [Z_e, V_{dq}, \beta_{ext}, R]$ to represent the radar and lidar measurements, vector $\mathbf{x} = [A_s, Dg_s, A_l, Dg_l]$ to stand for PSD parameters that need to be retrieved, vector $\mathbf{m} = [a_{ms}, b_{ms}, a_{ml}, b_{ml}, a_{as}, b_{as}, a_{al}, b_{al}]$ to stand for the empirically derived model parameters and **F** to represent the forward model equations, the problem can be symbolically expressed as:

$$\mathbf{d} = \mathbf{F}(\mathbf{x}, \mathbf{m}) \tag{2.24}$$

Our objective is to estimate the PSD parameters by solving the inverse problem expressed as:

$$\mathbf{x} = \mathbf{F}^{-1}(\mathbf{d}, \mathbf{m}) \tag{2.25}$$

Since only three measurements are available to retrieve four unknowns, the inverse problem represented by Equation (2.25) is ill-posed and a particular solution for **x** may

not be unique. Therefore, care must be taken to find an optimal solution based on certain criteria. The optimal estimation method being used to solve the inverse problem, the derivation of initial guesses, and problems in the implementation is discussed next.

2.3.1 Optimal Estimation Method

One way to have an optimal estimate of **x** is to maximize the a posterior probability $P(\mathbf{x}\,|\,\mathbf{d})$, which is the conditional probability of **x** given **d**. According to Bayes' theorem, $P(\mathbf{x}\,|\,\mathbf{d})$ can be expressed as:

$$P(\mathbf{x}\,|\,\mathbf{d}) = \frac{P(\mathbf{d}\,|\,\mathbf{x})P(\mathbf{x})}{P(\mathbf{d})} \tag{2.26}$$

where $P(\mathbf{d})$ only acts as a normalizing constant, $P(\mathbf{x})$ is the prior probability describing the prior knowledge of vector $\mathbf{x}$, and $P(\mathbf{d}\,|\,\mathbf{x})$ is the probability of the measurement vector **d** given $\mathbf{x}$.

From Equation (2.26) we see that the maximization of $P(\mathbf{x}\,|\,\mathbf{d})$ can be achieved by maximizing the product of $P(\mathbf{d}\,|\,\mathbf{x})$ and $P(\mathbf{x})$.

Under a Gaussian distribution assumption, $P(\mathbf{d}\,|\,\mathbf{x})$ can be expressed as:

$$P(\mathbf{d}\,|\,\mathbf{x}) = \frac{|\mathbf{S}_\mathbf{d}|^{-1/2}}{(2\pi)^{N/2}} \exp[-\frac{1}{2}(\mathbf{d}-\bar{\mathbf{d}})^T \mathbf{S}_\mathbf{d}{}^{-1}(\mathbf{d}-\bar{\mathbf{d}})] \tag{2.27}$$

Then $P(\mathbf{x})$ can be written as:

$$P(\mathbf{x}) = \frac{|\mathbf{S}_a|^{-1/2}}{(2\pi)^{N/2}} \exp[-\frac{1}{2}(\mathbf{x}-\bar{\mathbf{x}})^T \mathbf{S}_a{}^{-1}(\mathbf{x}-\bar{\mathbf{x}})] \tag{2.28}$$

where $\bar{\mathbf{d}}$ and $\mathbf{S_d}$ are mean and covariance of vector $\mathbf{d}$; $\bar{\mathbf{x}}$ and $\mathbf{S}_a$ are mean and covariance of vector $\mathbf{x}$.

Since it is an underlying assumption in the measurement that the observed data $\mathbf{d}$ is the mean of all random processes being observed, Equation (2.24) only holds for the mean value, and it is rewritten as:

$$\bar{\mathbf{d}} = \mathbf{F}(\mathbf{x}, \mathbf{m}) \tag{2.29}$$

Substituting Equation (2.29) into Equation (2.27), we have:

$$P(\mathbf{d} \mid \mathbf{x}) = \frac{|\mathbf{S_d}|^{-1/2}}{(2\pi)^{N/2}} \exp[-\frac{1}{2}(\mathbf{d}-\mathbf{F}(\mathbf{x}, \mathbf{m}))^T \mathbf{S_d}{}^{-1}(\mathbf{d}-\mathbf{F}(\mathbf{x}, \mathbf{m}))] \tag{2.30}$$

Using the a priori guess $\mathbf{x}_a$ as the mean of $\mathbf{x}$, we have the analytical expression for $P(\mathbf{x})$:

$$P(\mathbf{x}) = \frac{|\mathbf{S}_a|^{-1/2}}{(2\pi)^{N/2}} \exp[-\frac{1}{2}(\mathbf{x}-\mathbf{x}_a)^T \mathbf{S}_a{}^{-1}(\mathbf{x}-\mathbf{x}_a)] \tag{2.31}$$

From Equations (2.30) and (2.31), the product of $P(\mathbf{d} \mid \mathbf{x})$ and $P(\mathbf{x})$ is

$$P(\mathbf{d}\mid\mathbf{x})P(\mathbf{x})=\frac{\left|\mathbf{S_d}\mathbf{S}_a\right|^{-1/2}}{(2\pi)^N}\exp\{-\frac{1}{2}[(\mathbf{d}-\mathbf{F}(\mathbf{x},\mathbf{m}))^T\mathbf{S_d}^{-1}(\mathbf{d}-\mathbf{F}(\mathbf{x},\mathbf{m}))+(\mathbf{x}-\mathbf{x}_a)^T\mathbf{S}_a{}^{-1}(\mathbf{x}-\mathbf{x}_a)]\} \tag{2.32}$$

From Equation (2.32) we can see that to maximize the product of $P(\mathbf{d}\mid\mathbf{x})$ and $P(\mathbf{x})$, we just need to minimize the following cost function.

$$f(\mathbf{x})=(\mathbf{d}-\mathbf{F}(\mathbf{x},\mathbf{m}))^T\mathbf{S_d}^{-1}(\mathbf{d}-\mathbf{F}(\mathbf{x},\mathbf{m}))+(\mathbf{x}-\mathbf{x}_a)^T\mathbf{S}_a{}^{-1}(\mathbf{x}-\mathbf{x}_a) \tag{2.33}$$

To find the vector **x** that minimizes Equation (2.33), the first derivative of the cost function is first set to zero, and then solved for **x**:

$$\mathbf{x}=\mathbf{x}_a+\mathbf{S}_a\mathbf{K_x}^T\mathbf{S_d}^{-1}(\mathbf{d}-\mathbf{F}(\mathbf{x},\mathbf{m})) \tag{2.34}$$

where $\mathbf{K_x}$ is the Jacobian matrix that represents the sensitivity of the forward model to the PSD parameters being retrieved:

$$\mathbf{K_x}=\frac{\partial\mathbf{F}}{\partial\mathbf{x}}=\begin{bmatrix}\frac{\partial Z_e}{\partial A_l} & \frac{\partial Z_e}{\partial D_{gl}} & \frac{\partial Z_e}{\partial A_s} & \frac{\partial Z_e}{\partial D_{gs}}\\ \frac{\partial V_{dq}}{\partial A_l} & \frac{\partial V_{dq}}{\partial D_{gl}} & \frac{\partial V_{dq}}{\partial A_s} & \frac{\partial V_{dq}}{\partial D_{gs}}\\ \frac{\partial \beta_{ext}}{\partial A_l} & \frac{\partial \beta_{ext}}{\partial D_{gl}} & \frac{\partial \beta_{ext}}{\partial A_s} & \frac{\partial \beta_{ext}}{\partial D_{gs}}\\ \frac{\partial R}{\partial A_l} & \frac{\partial R}{\partial D_{gl}} & \frac{\partial R}{\partial A_s} & \frac{\partial R}{\partial D_{gs}}\end{bmatrix} \tag{2.35}$$

Since the solution for **x** is not explicitly expressed in Equation (2.34), this equation

must be solved numerically. Assuming the inverse problem is not too nonlinear, the Gauss-Newton method can be used to solve Equation (2.34) numerically, and the iteration formulation is expressed in Equation (2.36).

$$\mathbf{x}_{i+1} = \mathbf{x}_i + (\mathbf{S}_a^{-1} + \mathbf{K}_\mathbf{x}^T \mathbf{S}_\mathbf{d}^{-1} \mathbf{K}_\mathbf{x})^{-1} [\mathbf{K}_\mathbf{x}^T \mathbf{S}_\mathbf{d}^{-1} (\mathbf{d} - \mathbf{F}(\mathbf{x}_i, \mathbf{m})) - \mathbf{S}_a^{-1} (\mathbf{x}_i - \mathbf{x}_a)] \tag{2.36}$$

In sum, the solution for **x** can be derived by maximizing the a posteriori probability $P(\mathbf{x} \mid \mathbf{d})$, which is the probability of the PSD parameters given a set of observations. The optimal solution from Bayes' theorem is, therefore, a Maximum A Posteriori (MAP) solution. Since under a Gaussian PDF assumption, a MAP solution is equivalent to a minimum variance solution (Zhdanov, 2003), the optimal estimation solution should minimize the misfit between **F**(**x,m**) and **d**, meaning that a global minimum of the misfit should be found. However, the above conclusions are correct only under the assumption that the inverse problem is moderately nonlinear, because in the derivation of Equation (2.36), only the first derivative is preserved and all higher order derivative terms are ignored. The linear assumption and the ill posed nature of the problem represent significant challenges for this algorithm as discussed in the following.

2.3.2 Initial Guess

To use the Gauss Newton iterative scheme discussed above, very realistic initial guesses of the PSD parameters need to be derived first so that the iteration begins with values that are fairly close to the actual values. Because the radar measurements are weighted more to the larger particles in the PSD, it is reasonable to initially neglect the

contribution from small particles in order to calculate the initial guesses of the large mode parameters A_l and D_{gl}.

Since the large particle Doppler fall speed in quiet air V_{dql} dominates the total Doppler fall speed V_{dq}, V_{dq} is approximately equal to V_{dql}, and from the forward model Equation (2.18), the initial guess of D_{gl} can be expressed in terms of V_{dq} as:

$$Dg_{Li} = \left[\frac{V_{dq}\Gamma(\alpha_l + b_{zl} + 7)}{a_{vl}\Gamma(\alpha_l + b_{zl} + b_{vl} + 7)} \right]^{\frac{1}{b_{vl}}} \tag{2.37}$$

Similar to the initial guess of parameter D_{gl}, the initial guess of parameter A_l can be calculated from the forward model Equation (2.17) by neglecting the radar reflectivity contribution from small particles, and it can be written as:

$$A_{Li} = \frac{Z_e}{ea_{zl} Dg_{Li}^{\,b_{zl}+7}\Gamma(\alpha_l + b_{zl} + 7)} \tag{2.38}$$

Substituting Equation (2.37) into Equation (2.38), the initial guess of parameter A_l can be expressed by radar reflectivity factor Z_e and the terminal fall velocity V_{dq} as:

$$A_{Li} = \frac{Z_e}{ea_{zl}\Gamma(\alpha_l + b_{zl} + 7)} \left[\frac{V_{dq}\Gamma(\alpha_l + b_{zl} + 7)}{a_{vl}\Gamma(\alpha_l + b_{zl} + b_{vl} 7)} \right]^{-\frac{b_{zl}+7}{b_{vl}}} \tag{2.39}$$

After the initial guesses of large mode parameters A_l and D_{gl} are derived, the large mode lidar extinction can be calculated according to forward model Equation (2.19):

$$\beta_{extl} = 2A_l ea_{al} Dg_l^{b_{al}+1} \Gamma(\alpha_l + b_{al} + 1) \tag{2.40}$$

Then, we can difference the Raman lidar extinction from the calculated large mode extinction to get the small mode lidar extinction. Finally, temporarily keeping the initial guess of D_{gs} as a constant, we can calculate the initial guess of parameter A_s by the following equation:

$$A_{si} = \frac{\beta_{ext} - \beta_{extl}}{2ea_{as} Dg_s^{b_{as}+1} \Gamma(\alpha_s + b_{as} + 1)} \tag{2.41}$$

Now, with one initial guess D_{gs} fixed as a constant temporarily, the initial guesses of three PSD parameters A_l, D_{gl} and A_s are calculated from Z_e, V_{dq} and β_{ext}. The procedure is summarized in Figure 2.

2.3.3 Two Problems in the Implementation

In the implementation of the ideas discussed above, two problems need to be solved in the retrieval algorithm.

First, in the derivation of the initial guesses of the PSD parameters, it is possible that the large mode optical extinction calculated from the radar measurements is greater than the total extinction estimated by the Raman lidar measurement. Considering the instrument error in the radar and lidar measurements, and the assumptions made in the

forward model and the empirically derived power-law coefficients, this is a reasonable occurrence and it suggests that a single PSD mode can be assumed when the difference between the calculated and measured extinction is smaller than the combined error. In other words, because a prominent small PSD mode would contribute significantly to the extinction but not the radar measurements, a bimodal assumption is not needed when the radar measurements can be used to reasonably approximate the measured lidar extinction. When this situation is found, we implement an algorithm that uses three radar and lidar measurements – radar reflectivity, Doppler velocity and lidar extinction, to retrieve a single mode PSD but with three free parameters A, D_g and α. The details of this algorithm including the forward model equations are described in Appendix A: single mode retrieval algorithm.

A second problem arises because only the lidar extinction is available to calculate two small mode PSD parameters in the initial guesses, requiring us to fix either D_{gs} or A_s. The algorithm is quite sensitive to this choice because the cost function has several local minima, and the Gauss Newton method is formulated to find an optimal solution for a problem that is not very nonlinear (i.e., where a global minimum of the cost function is easily identified).

So if the initial guess is not set properly, the Gauss Newton method reaches a local minimum instead of the global minimum. For example, the sensitivity of the retrieval results to parameter D_{gs} can be examined by using radar and lidar data simulated from the forward model while fixing parameters A_l and D_{gl}.

The contour of the misfit, which is the mean squared error (MSE) of the retrieved radar and lidar data, is shown in Figure 3.

In Figure 3, we see several local minima with very small misfit that could be identified by the optimal estimation method. Since the Gauss Newton method is simply designed to identify a zero gradient condition, if the parameter D_{gs} is initially set to a value that is not close to the actual solution, the Gauss Newton method could converge to one of these local minima instead of the global minimum.

One simple and approximate solution to this problem is to iterate on the initial guess of D_{gs} within a range of values, perform the algorithm using every initial guess, and choose the one with the minimum misfit as the initial guess to be used in the retrieval algorithm. After using this method, the accuracy of the retrieval algorithm is greatly improved. The difference of particle size distribution retrievals before and after using this method is shown in Figure 4.

This approach increases the computational expense of the algorithm. However, it greatly increases the algorithm accuracy, and makes the algorithm capable of retrieving high concentrations of small particles when appropriate.

2.4 Retrieval Uncertainty Evaluation

An optimal solution and solution uncertainty are two fundamental requirements for an inverse method (Wunsch, 2006). So a retrieval algorithm should not only be able to give optimal estimates of desired quantities, but also provide estimation of how accurate the retrieved quantities are. Rodgers (2000) shows that retrieval algorithm error sources can be classified into four types: smoothing error, forward model error, model parameter error, and measurement error.

According to Rodgers (2000), the smoothing error refers to the loss of information

from remote sensing systems' inability to see fine spatial structure. Since the actual statistics of the fine structure being observed by Doppler radar and Raman lidar are unknown, the retrieval here is an estimate of a smoothed version of the cloud state, instead of an estimate of the complete state. So the smoothing error is not quantified here.

The forward model error is due to the approximations in the forward model assumptions. For this study, they include the bimodal particle size distribution assumptions, and also the Rayleigh scattering and Mie scattering assumptions used in the forward model equations. Since the Rayleigh scattering and Mie scattering assumptions are valid for 35 GHz radar and Raman lidar in measuring cirrus cloud reflectivity and extinction as discussed before, the errors from Rayleigh and Mie scattering assumptions should be small enough to be neglected.

For the error from the PSD assumption, DM06 shows that the two-parameter PSD functions including exponential and gamma functions are applicable to retrieve particle sizes when the actual PSD is not significantly bimodal. The two gamma functions are sufficient to represent a small mode and a large mode PSD. The error from the bimodal PSD model should also be small when the actual PSD is significantly bimodal.

In sum, the errors from bimodal PSD model assumptions and forward model assumptions are both assumed small in this study relative to the known uncertainties in the model parameters and measurements, so the forward model error is not considered here either. In the following the retrieval errors from measurements and the empirical model parameters are shown to be two major error sources, and they are discussed in detail.

2.4.1 Measurement Error

The total measurement error includes systematic error (due to instrument calibration) and measurement noise, which is assumed to be random and unbiased. For radar reflectivity, based on a known uncertainty in the MMCR radar reflectivity of approximately 1-2 dBZ (Clothiaux et al., 1999; Miller, personal communication, 2001), a 25% error is applied to the radar reflectivity. Since the terminal fall velocity V_{dq} is from the retrieval of DM06 and their uncertainty estimation of retrieved V_{dq} is about 30%, this value is directly used as the measurement error for V_{dq} in the error analysis.

Compared to radar measurement error, the measurement error for the lidar extinction is quite variable; it strongly depends on factors like signal to noise ratio, laser power fluctuations, and also the time of day (day time or night time). Since the error of the extinction is estimated when the extinction is derived from the Raman lidar measurements, the estimated error for lidar extinction is used in the algorithm. However, to have a general idea of how accurate the derived lidar extinction is, the averaged extinction error is calculated by using one year's data, and it is about 8.9% for daytime and about 6.7% for night time.

Once we have the estimates of the uncertainties in Z_e, V_{dq} and β_{ext}, assuming no correlation between these measurement errors, the measurement error covariance matrix S_ε can be written:

$$S_\varepsilon = \begin{bmatrix} \delta_z & 0 & 0 \\ 0 & \delta_{vdq} & 0 \\ 0 & 0 & \delta_\beta \end{bmatrix} \tag{2.42}$$

where δ_z, δ_{vdq} and δ_β are the uncertainties for Z_e, V_{dq} and β_{ext} respectively.

2.4.2 Power Law Model Parameter Error

As mentioned in forward model equations, to express the radar and lidar measurements as functions of PSD parameters only, six empirically derived power law model parameters are used in the forward model equations, which are mass-dimensional power law coefficients a_m, b_m, area-dimensional power law relationship coefficients a_a, b_a, and terminal fall velocity parameters a_v, b_v.

These model parameters are primarily dependent on the particle habits, and substantial variations exist in these parameters when assuming different particle habits. For example, a_z and b_z are power law parameters to fit the radar backscattering cross section from ice crystals with a certain shape. They can be derived from the mass-dimensional power law coefficients a_m, b_m as shown in DM06. To see how well the radar cross section (RCS) power-law fit is, the radar cross section $\sigma(D)$ for a certain ice crystal shape can be first calculated by using the Discrete Dipole Approximation (DDA) method (Donovan et al., 2004; Liu, 2008) so that the RCS from power-law empirical parameters can be compared with the numerical computation results. The comparison of the radar cross section from power law fit and from the numerical method is shown in Figure 5. From Figure 5, we see that the power law fit generally agrees well with the numerical results. However, this agreement only happens when the particle habit is unique and the same as what is used in the numerical computation. Since the ice crystal habit in cirrus is not unique, and often is unknown, the error from these empirically derived power law parameters used in the algorithm needs to be quantified.

To have a reasonable estimation of the errors in these parameters, the standard deviations of the model parameters for different particle habits, as found in Mitchell (1996), are used as the uncertainties of these model parameters.

In the calculation of the standard deviation, different particle habit groups are used for the small mode and the large mode of the size distribution, considering the different habits that the small and large particles may have. Specifically, five particle habits, which include hexagonal plates, hexagonal columns, crystal with sector-like branches, broad-branched crystal, and stellar crystal with broad arms are chosen for the small mode. The mass- and area-dimensional model parameters a_m, b_m, a_a and b_a for the small mode are listed in Table 1. Particle habits including hexagonal columns, side planes, bullet rosettes with five branches, aggregates of side planes, columns and bullets are used for the large mode. The mass- and area-dimensional model parameters for large mode are listed in Table 2.

Because parameters a_v and b_v can be derived from the air density, kinematic viscosity and parameters a_m, b_m, a_a, b_a, as shown in Equations (2.10) and (2.11), and because parameters a_z and b_z can be expressed by the parameters a_m and b_m, as shown in Equations (2.5) and (2.6), only the standard deviations for parameters a_m, b_m, a_a, b_a need to be calculated for both the small mode and the large mode, which are listed in Table 3.

Once the standard deviations for each model parameter are calculated, the model parameter error covariance matrix $\mathbf{S_m}$ can be written as:

$$\mathbf{S_m} = \begin{bmatrix} \delta_{a_m} & 0 & 0 & 0 \\ 0 & \delta_{b_m} & 0 & 0 \\ 0 & 0 & \delta_{a_a} & 0 \\ 0 & 0 & 0 & \delta_{b_a} \end{bmatrix} \tag{2.43}$$

where δ_{a_m} is a matrix $\begin{bmatrix} \delta_{a_{ms}} & 0 \\ 0 & \delta_{a_{ml}} \end{bmatrix}$, including the standard deviations for the small mode parameter a_{ms} and the large mode parameter b_{ms}, and the same for δ_{b_m}, δ_{a_a}, δ_{b_a}.

2.4.3 Retrieval Error Estimation

Since the measurement error and the model parameter error are the two major errors, Bayes' theorem is used to quantify the retrieval error from these two error sources.

Following the derivation in Rodgers (2000), once the measurement error covariance matrix $\mathbf{S}_\varepsilon$ and the model parameter error covariance matrix $\mathbf{S_m}$ are given, the retrieval error $\mathbf{S_x}$ from $\mathbf{S_\varepsilon}$ and $\mathbf{S_m}$ can be derived as:

$$\mathbf{S_x} = \left(\mathbf{K_x}^T \mathbf{S_d}^{-1} \mathbf{K_x} + \mathbf{S}_a^{-1}\right)^{-1} \tag{2.44}$$

In Equation (2.44), $\mathbf{S_d}$ is the total error covariance matrix, which includes the instrument error covariance matrix $\mathbf{S}_\varepsilon$ and model parameter error covariance matrix S_m, and it is written as:

$$\mathbf{S_d} = \mathbf{S_\varepsilon} + \mathbf{K_m S_m K_m}^T \tag{2.45}$$

where $\boldsymbol{K_m}$ is the Jacobian matrix representing the sensitivity of the forward model to

model parameters, and is written as:

$$\mathbf{K_m} = \frac{\partial \mathbf{F}}{\partial \mathbf{m}} = \begin{bmatrix} \frac{\partial Z_e}{\partial a_{ms}} & \frac{\partial Z_e}{\partial b_{ms}} & \frac{\partial Z_e}{\partial a_{ml}} & \frac{\partial Z_e}{\partial b_{ml}} & \frac{\partial Z_e}{\partial a_{as}} & \frac{\partial Z_e}{\partial b_{as}} & \frac{\partial Z_e}{\partial a_{al}} & \frac{\partial Z_e}{\partial b_{al}} \\ \frac{\partial V_{dq}}{\partial a_{ms}} & \frac{\partial V_{dq}}{\partial b_{ms}} & \frac{\partial V_{dq}}{\partial a_{ml}} & \frac{\partial V_{dq}}{\partial b_{ml}} & \frac{\partial V_{dq}}{\partial a_{as}} & \frac{\partial V_{dq}}{\partial b_{as}} & \frac{\partial V_{dq}}{\partial a_{al}} & \frac{\partial V_{dq}}{\partial b_{al}} \\ \frac{\partial \beta_{ext}}{\partial a_{ms}} & \frac{\partial \beta_{ext}}{\partial b_{ms}} & \frac{\partial \beta_{ext}}{\partial a_{ml}} & \frac{\partial \beta_{ext}}{\partial b_{ml}} & \frac{\partial \beta_{ext}}{\partial a_{as}} & \frac{\partial \beta_{ext}}{\partial b_{as}} & \frac{\partial \beta_{ext}}{\partial a_{al}} & \frac{\partial \beta_{ext}}{\partial b_{al}} \\ \frac{\partial R}{\partial a_{ms}} & \frac{\partial R}{\partial b_{ms}} & \frac{\partial R}{\partial a_{ml}} & \frac{\partial R}{\partial b_{ml}} & \frac{\partial R}{\partial a_{as}} & \frac{\partial R}{\partial b_{as}} & \frac{\partial R}{\partial a_{al}} & \frac{\partial R}{\partial b_{al}} \end{bmatrix} \tag{2.46}$$

In sum, in the algorithm we give a large uncertainty (100%) to the a priori of all PSD parameters, 25% uncertainty to radar reflectivity, 30% to terminal fall velocity, 15% to optical extinction, and use the standard deviations listed in Table 3 as the uncertainties for power law model parameters. As an example, if we take a typical set of measurements, **d**=[-30.23, 44.80, 0.15], as the input of the algorithm, the theoretical estimation of the covariance matrix of the retrieval solution $\mathbf{S_x}$ is:

$$\mathbf{S_x} = \begin{bmatrix} 0.921 & 0 & 0 & 0 \\ 0 & 0.396 & 0 & 0 \\ 0 & 0 & 0.842 & 0 \\ 0 & 0 & 0 & 0.314 \end{bmatrix} \tag{2.47}$$

So the relative retrieval errors of retrieved PSD parameters A_s, D_{gs}, A_l, D_{gl} are 92.1%, 39.6%, 84.2% and 31.4%, respectively.

To see how much the retrieval error is attributable to empirical relationships and how

much is due to measurement errors, a sensitivity test of the retrieval algorithm error to the empirical relationships and measurement errors is given next.

2.4.4 Sensitivity Test

From Equation (2.44), we see that the covariance of the solution vector $\boldsymbol{x}$ is determined by the covariance of the measurement vector $\boldsymbol{d}$ and the covariance of the empirical model parameter vector $\boldsymbol{m}$. So the retrieval sensitivity to the measurement error and the model parameter error are tested respectively in the following.

First, the sensitivity of the retrieval error to the model parameter error is tested by varying the model parameter error and fixing the measurement error to 5%. Using the same radar and lidar measurements mentioned above as the input of the algorithm, the retrieval errors of four PSD parameters are given by Equation (2.44), and the errors of IWC, and maximum dimension D_m can be calculated from Equations (2.21) and (2.22). The retrieval errors from different modal parameter errors are listed in Table 4.

From Table 4, we can see, as the modal parameter covariance increases from 5% to 100%, the retrieval errors of all PSD parameters are increasing. The retrieval error of D_m increases from 16.6% to 72.4%, and the retrieval error of IWC increases from 77.5% to 233.7%.

Fixing the model parameter covariance to 5%, and varying the measurement error, the retrieval sensitivity to measurement errors is also tested. The retrieval error for D_m increases from 16.6% to 21.9%, and the retrieval error for IWC increases from 77.5% to 112.8%, as the measurement covariance increases from 5% to 100%.

The retrieval errors from different measurement errors are listed in Table 5, and the

retrieval errors of the PSD with different measurement and model parameter covariance are shown in Figure 6. From Figure 6 and the comparison of Table 4 and Table 5, we find that the retrieval errors are more sensitive to the uncertainty in empirical parameters than to reasonable uncertainties in the measurements.

Table 1. Coefficients and exponents of mass-dimensional and area-dimensional relationships for small mode.

Particle Type	Mass		Area	
	a_m	b_m	a_a	b_a
Hexagonal Columns	0.1677	2.91	0.684	2.0
Bullet rosettes	0.00308	2.26	0.0869	1.57
Hexagonal Plates	0.00739	2.45	0.24	1.85
Crystal with branches	0.00614	2.42	0.24	1.85
Broad-branched Crystal	0.00583	2.42	0.24	1.85

Table 2. Coefficients and exponents of mass-dimensional and area-dimensional relationships for large mode.

Particle Type	Mass		Area	
	a_m	b_m	a_a	b_a
Hexagonal Columns	0.000907	1.74	0.0512	1.414
Side Planes	0.00419	2.3	0.2285	1.88
Bullet rosettes	0.00308	2.26	0.0869	1.57
Aggregates	0.0028	2.1	0.2285	1.88
Hexagonal Plates	0.00739	2.45	0.65	2.0

Table 3. Means and standard deviations of mass-dimensional and area-dimensional power law parameters.

	Mean	Standard deviation	Normalized STD
a_{ms}	0.0380	0.0649	1.7054
b_{ms}	2.4920	0.2453	0.0984
a_{as}	0.2982	0.2256	0.7567
b_{as}	1.8240	0.1561	0.0856
a_{ml}	0.0037	0.0024	0.6506
b_{ml}	2.1700	0.2707	0.1248
a_{al}	0.2490	0.2382	0.9567
b_{al}	1.7488	0.2458	0.1405

Table 4. Sensitivity of retrieved PSD parameters to uncertainty in empirical relationships (5% S_ε ,100% S_a).

	Retrieval errors (%)					
S_m	A_s	D_{gs}	A_l	D_{gl}	IWC	D_m
5%	72.3	18.8	60.2	19.9	77.5	16.6
10%	87.0	22.4	78.8	30.9	116.3	25.4
50%	97.6	25.5	95.4	73.4	217.3	60.1
100%	98.3	26.5	97.3	90.0	233.7	72.4

Table 5. Sensitivity of retrieved PSD parameters to uncertainty in measurements (5% S_m , 100% S_a).

S_ε	Retrieval errors (%)					
	A_s	D_{gs}	A_l	D_{gl}	IWC	D_m
5%	72.3	18.8	60.2	19.9	77.5	16.6
10%	76.9	20.1	60.9	20.1	78.2	16.7
50%	93.1	23.6	75.4	22.6	94.7	18.2
100%	96.2	24.4	87.3	27.3	112.8	21.9

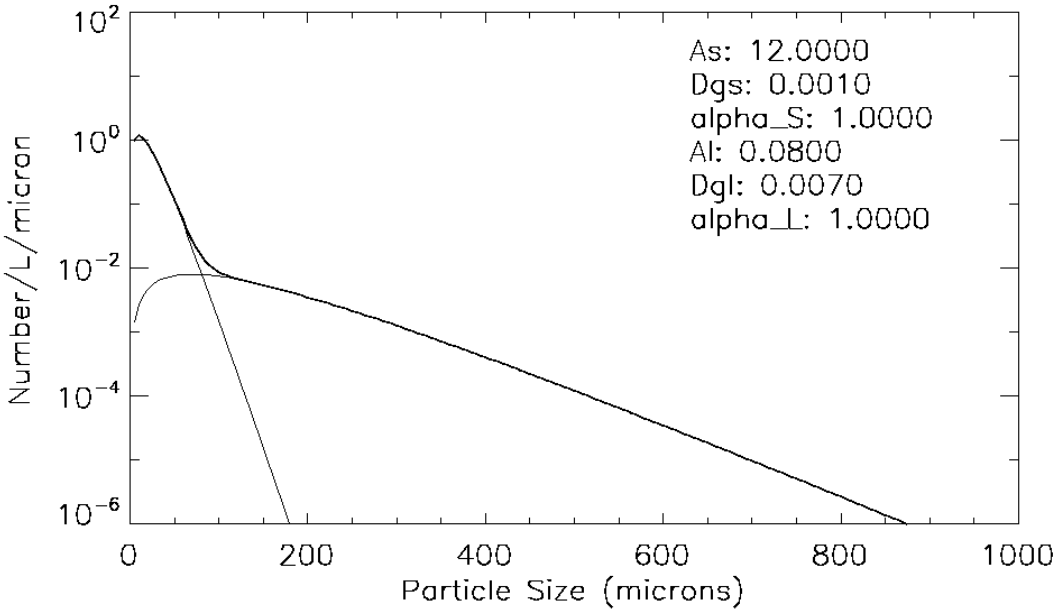

Figure 1. A bimodal particle size distribution with six parameters (Three parameters A_s, Dg_s, α_s control the small mode distribution, the other three parameters A_l, Dg_l, α_l control the large mode distribution).

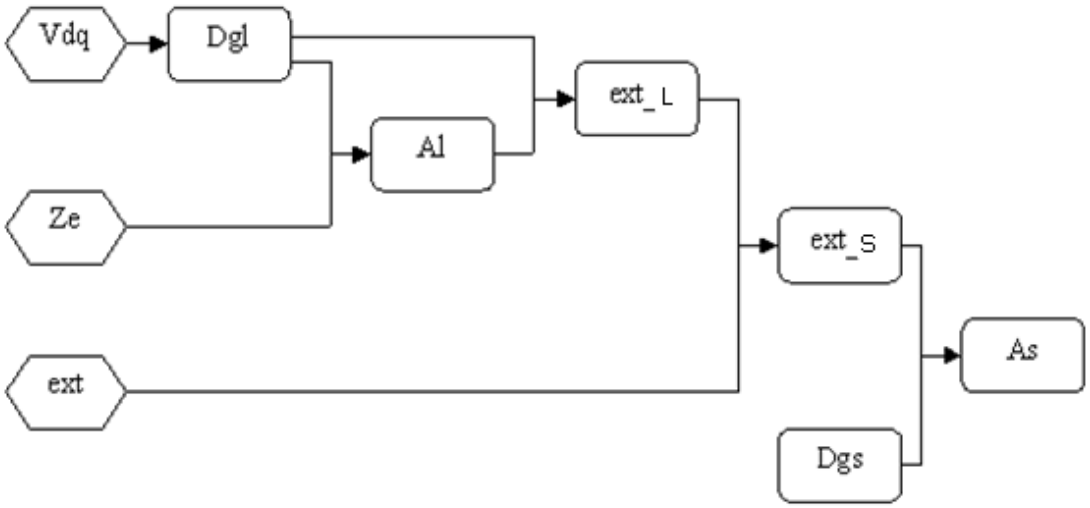

Figure 2. Flowchart of the derivation of the initial guesses.

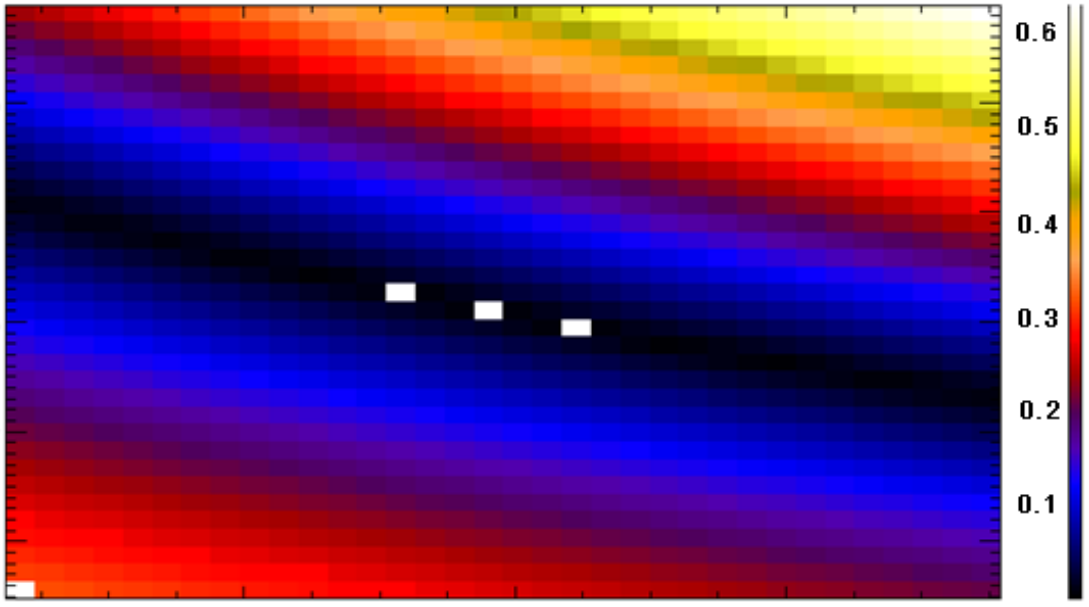

Figure 3. Contour of the misfit function.

(The black areas are local minima with misfit less than 0.1 and three white squares stand for two strong local minima with misfit less than 0.002 and one global minimum with misfit of $1.6e^{-6}$)

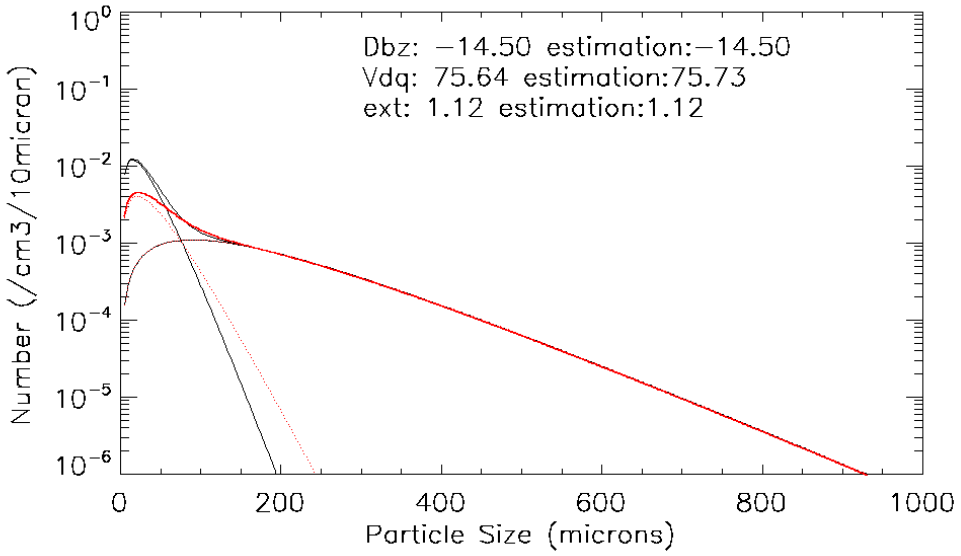

(a) Before improvement in algorithm

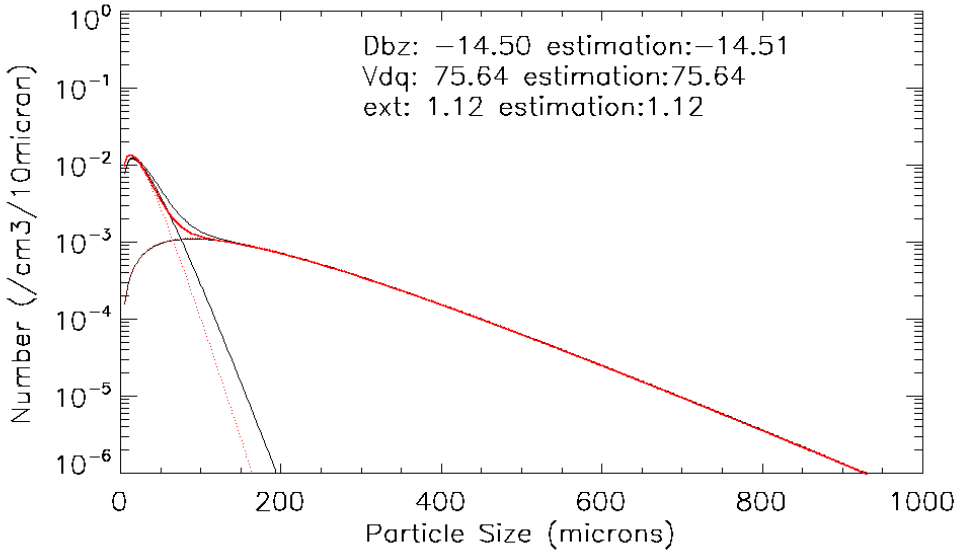

(b) After improvement in algorithm

Figure 4. PSD retrievals comparison.

(Before improvement (a); after improvement (b); red: retrieved PSD; black: true PSD)

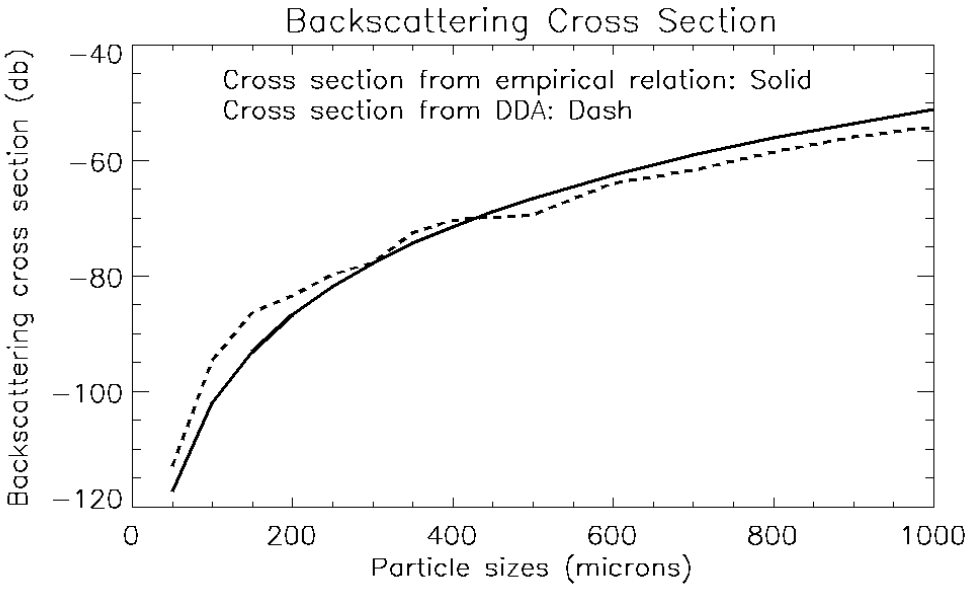

Figure 5. Radar backscattering cross section from DDA and empirical relation.

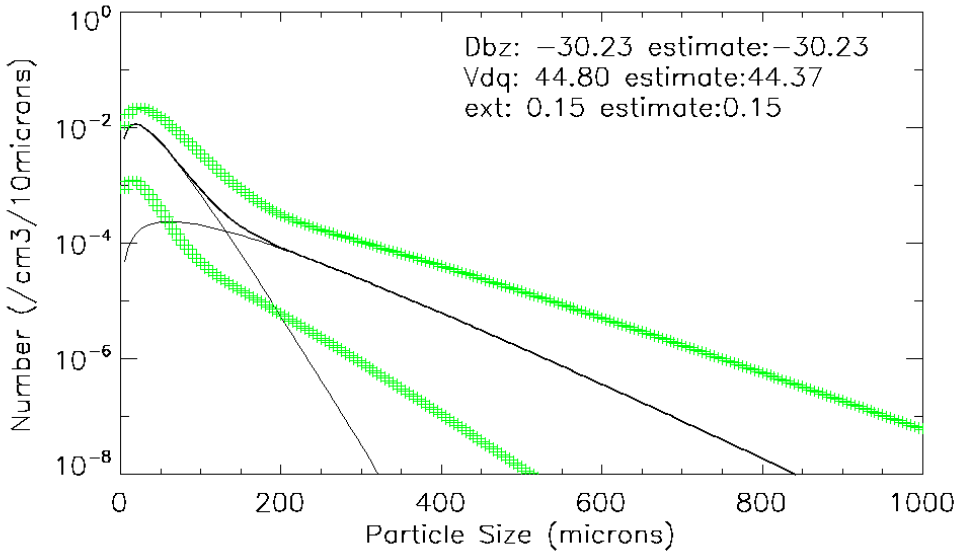

(a) 10% measurement error, 10% empirical parameters error

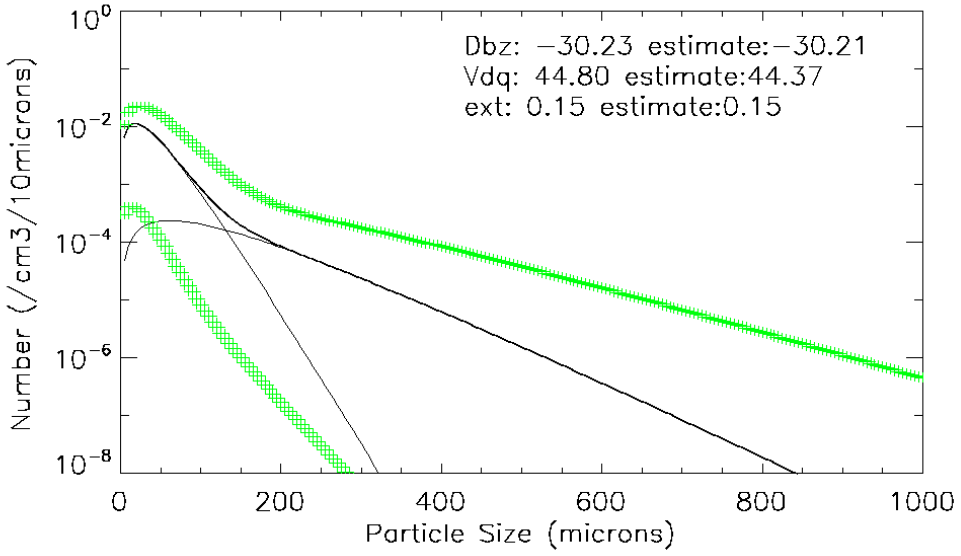

(b) 10% measurement error, 30% empirical parameters error

Figure 6. Examples of PSD retrieval uncertainty due to empirical relationship. (solid line: retrieval result; pluses: uncertainty of PSD retrieval)

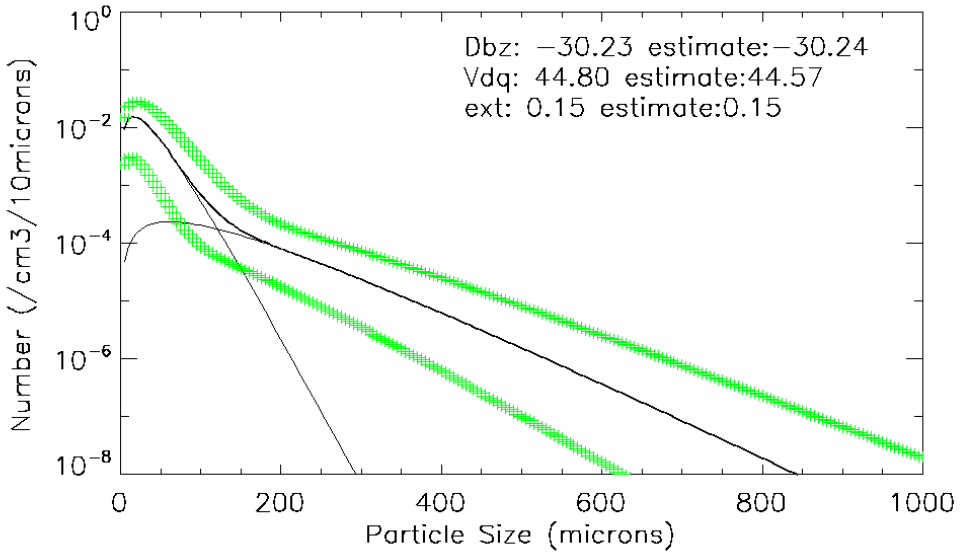

(c) 5% empirical parameters error, 10% measurement error

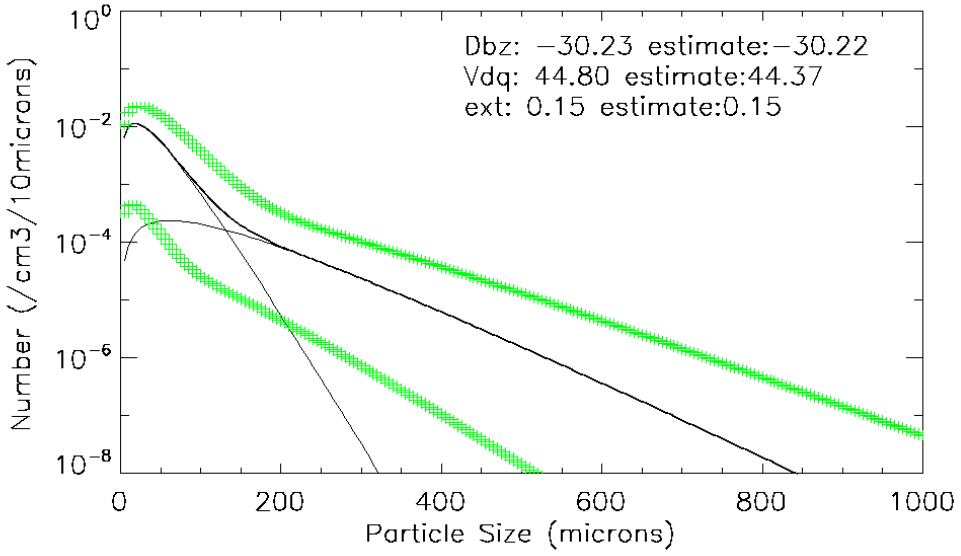

(d) 5% empirical parameters error, 100% measurement error

Figure 6. continued.

CHAPTER 3

CASE STUDY

In this chapter, the in situ measurements including the concentration and the IWC collected by airborne instruments on board the UND Citation during the 2000 Cloud IOP are used in the case study to compare with the retrievals from ground-based remote sensing measurements. A statistical approach is first introduced for the comparison of aircraft in situ measurements with retrieval from ground-based measurements to minimize the differences in sample volume, and time and space between the two platforms. Then the airborne instruments used in the case study and their problems are discussed. After that, the PSD retrievals from ground-based remote sensing measurements are compared with the PSD in situ measurements from the 2DC and the FSSP, and the IWC retrievals are compared with the IWC measured by the CVI.

3.1 Comparing In Situ Measurements with Ground-Based Retrievals

3.1.1 Difficulties in Comparison

Due to time, spatial and sample volume differences between the aircraft in situ measurements and the ground-based remote sensing measurements, comparing aircraft in situ measurements with retrievals from ground-based remote sensing measurements is challenging. The difficulties of comparing aircraft in situ measurements with ground-based remote sensing measurements are explored in earlier studies (e.g., Matrosov, 1997).

Here, the specific difficulties of comparing in situ measurements during horizontal flight legs with retrievals from vertically pointing remote sensors are summarized, and a method to overcome these difficulties is then proposed.

As mentioned in Mace et al. (2002), the sample volume of the MMCR at the ARM SGP site is about 77000 m^3 at 10 km. The sample volume rate of the PMS 2DC on the UND Citation is about 6 liter s^{-1}, so if using 5 seconds averages as is typical to get reasonable aircraft sample statistics in the in situ probes, the sample volume of the airborne instruments is only about 0.03 m^3 (30 liters). There are six orders of magnitude difference in the sample volumes between these two platforms for cirrus cloud at about 10 km altitude.

In addition to the large difference in sample volume, the spatial resolution of the aircraft in situ measurements during horizontal flight legs and that of the remote sensing measurements are also quite different. Specifically, for ground-based Raman lidar data, its time resolution is about 10 minutes because of the need to smooth the noisy molecular signal (Petty et al., 2006). Assuming that the cirrus clouds are moving at speeds of about 5-30 m s^{-1}, the horizontal spatial dimension of the Raman lidar ranges from 3 to 18 km. For the aircraft in situ measurements, assuming the aircraft is flying along a horizontal leg at a speed of about 100 m s^{-1}, the 5 seconds average of the in situ measurements would provide a horizontal spatial resolution of about 500 m. So depending on the wind speed and the aircraft speed, there exists a vast difference in horizontal spatial resolution between aircraft in situ data and the ground-based Raman lidar data.

Because of the differences of the sample volume and the spatial resolution between the airborne in situ measurements and the ground-based remote sensing measurements,

certain statistical approaches must be taken in order to make reasonable comparisons of data collected from the two platforms.

3.1.2 Statistical Method

The basic idea of this statistical approach relies on the fact that the aircraft flew horizontal legs along the ambient wind direction. We also assume that any changes that might occur between the time of measurement by the aircraft and when the remote sensors measured the volume can be neglected. In situ measurements sampled at a location that is more than 20 km away from the SGP site are not used in the comparison. We consider each aircraft measurement (5 seconds average) to constitute an independent sample and then we determine into which time-height remote sensing data bin the in situ measurement can be most reasonably placed. The in situ data in each remote sensing bin are then averaged to compare with the remote sensing retrieval. So the criteria used to match the in situ measurement with the remote sensing bin are most important in this statistical approach, and it is described in detail next.

First, since only the in situ measurements during horizontal legs are used in the comparison, all in situ measurements during the same horizontal leg are made at approximately a single altitude. After finding the average altitude of each leg, the in situ measurements in each leg will only be compared with remote sensing retrievals at the closest available range resolution volume. Because the vertical resolution of the MMCR is 90 meters, the largest possible vertical spatial difference between remote sensing retrievals and the aircraft in situ measurements is 45 m. In this way, measurements from the two platforms should be close to each other in the vertical direction.

Second, the in situ measurements should also be close enough to the remote sensing measurements in the horizontal plane. The coordinates of aircraft positions during the first five horizontal legs are recorded by the GPS system, and are shown in Figure 7. From Figure 7, we see that the UND Citation was flying close to the ARM SGP site (N36°37', W97°30') several times. The closest approach happened at 20:56 UTC, with a horizontal distance of 867 m from the aircraft to the SGP site. Although the aircraft never passed directly over the exact location of the SGP site during the flight, compared to the 3 km to 18 km horizontal resolution of Raman lidar, 867 m distance is close enough. This illustrates the difficulty of using high altitude aircraft to validate remote sensing measurements and why a statistical approach is necessary.

The third step is to minimize the time difference between these two platforms. In other words, we attempt to determine, given a time and location of in situ measurement, what time the aircraft resolution volume was in the vicinity of the SGP remote sensors. To be able to do that, the movement of the cirrus clouds is taken into account with the help of sounding data. Because of the 10 minutes time resolution of the Raman lidar, some part of the cloud sampled by the in situ instruments during the 10 minutes time period may flow out of the cloud area measured by the Raman lidar, and some that are sampled not during this 10 minutes may flow into the area, so the cloud movement must be taken into account. Assuming in a short time period, such as 10 minutes, the cloud system would only move with the wind without any significant changes in the cloud structure, then the same cloud sampled by the aircraft at time t_i will pass the SGP site at t_j or already passed the SGP site at t_k depending on whether the aircraft is upwind or downwind.

$$t_j = t_i + d/u \tag{3.1}$$

$$t_k = t_i - d/u \tag{3.2}$$

where u is the wind speed, which is acquired from interpolated sounding data, and d is the distance from the aircraft to the SGP site, which can be calculated as:

$$d = \sqrt{(2\pi R_1 cos\theta_s|\varphi - \varphi_s|/360)^2 + (2\pi R_2|\theta - \theta_s|/360)^2} \tag{3.3}$$

where R_1 and R_2 are the equatorial and polar radius of the Earth, respectively, θ_s and φ_s are the latitude and longitude of the SGP site, respectively, θ and φ are the latitude and longitude of the aircraft recorded by the GPS system.

By using the criteria discussed above, only the in situ measurements that are close both in time and space to the remote sensing measurements are averaged to compare with retrievals from the remote sensing measurements to account for the sampling difference between the two platforms.

A primary problem with this comparison approach is that it will not work on rapid change cloud systems, because in this approach, we assume that cirrus clouds do not have significant changes in the cloud structure during the 10-minute intervals. And also, this approach will not work on small scale cloud systems, because the horizontal scale of the 10-minute remote sensing intervals is on the order of km, not meters. So this method of comparing airborne in situ measurements with ground-based remote sensing retrievals is specifically designed for large horizontal scale cirrus cloud systems, in which case the

assumptions that we make in this approach are reasonable.

3.2 In Situ Measurements

In this case study, the in situ measurements collected by different airborne instruments on the UND Citation during the 2000 Cloud IOP are used. These instruments include the Cloud Particle Imager (CPI), the PMS 2DC, the FSSP and the CVI. All the aircraft instruments used in the case study are listed in Table 6; also listed are the in situ measurements made by these airborne instruments. The measurements from these airborne instruments and the problems in the measurements will be discussed in this section.

3.2.1 Particle Images from the CPI

The CPI images cloud particles in the size range of 20-2500 microns (maximum dimension), with an image resolution of 2.3 micron. So from the analysis of the particle images recorded by the CPI, the major particle habit of a cloud system can be deduced. For example, based on the images taken by the CPI on March 9th, 2000, bullet rosettes are found to be the predominant particle habit for the cirrus system on that day (Lewis et al., 2001). Once the major particle habit is known, the corresponding mass- and area-dimensional power law parameters will be used in the algorithm to retrieve the microphysical properties including the particle number concentration and IWC to compare with the in situ measurements.

3.2.2 Number Concentration from the 2DC and the FSSP

One important in situ measurement to be verified by remote sensing retrievals is the particle number concentration. The concentration in the range of 60-1500 μm is provided by the PMS 2DC, and the concentration in the range of 2-47 μm can be provided by the FSSP.

A problem with the PMS 2DC is the missampling of larger crystals due to the small collection area of the instruments (Gayet et al., 1993). Because the concentrations of larger particles in most thin cirrus clouds are very low, the PMS 2DC sample volume is so small that the 2DC sensor may not have enough sample statistics, and thus may greatly undercount the larger particles in its small sample volume. So it is a common approach to average the individual samples of 2DC over a certain time period to improve the sampling statistics. Five seconds is typically used to get reasonable sample statistics for larger cirrus particles.

For the FSSP, the shattering effect on the concentration measurements of small particles is discussed extensively in several recent papers (Heymsfield, 2007; McFarquhar et al., 2007). Two possible physical mechanisms were proposed for the particle shattering (Korolev and Isaac, 2005), and some studies used satellite retrievals to show that the measurements from the FSSP may be biased due to the particle shattering. However, since one motivation of this study is to see if the measurements from the FSSP are biased or not, the original in situ measurements from the FSSP will be directly used without any correction and compared with remote sensing retrievals.

3.2.3 Ice Water Content from the CVI

Besides the measurements of the number concentration, the Ice Water Content (IWC) was measured by the Counterflow Virtual Impactor (CVI) during the 2000 Cloud IOP. The CVI uses a counterflow stream of gas to separate cloud droplets or ice crystals from the interstitial aerosol and water vapor. The details of this instrument can be found in Twohy et al. (1997).

One issue that would affect the accuracy of the IWC measurements from the CVI is that there is a minimum size of ice particle that can penetrate the counterflow and penetrate the inside of the CVI inlet. As mentioned in Twohy et al. (1997), the minimum size of a cloud particle that is able to enter the CVI inlet tip is dependent on particle velocity, inlet size, and the CVI counterflow rate. The minimum particle diameter collected with 50% efficiency, also known as the "cut size" is about 7 microns aero-dynamic diameter (diameter of a unit-density sphere) for the NCAR CVI at sea level. According to Twohy et al. (2003), the cut sizes of the CVI at the airspeeds of 100 and 67 m s^{-1} are 8.2 and 9.6 microns aero-dynamic diameter, respectively.

To have an idea about the corresponding cut sizes in maximum dimension (D) as used in the retrieval algorithm, the aerodynamic diameter (D_a) can be converted to the maximum dimension (D) by the formalism in Appendix B.

According to Equation (B4) in Appendix B, using 0.91 g cm^{-3} as the unit density for solid ice sphere, and using the effective density versus D relationship representing the rosettes from Heymsfield et al. (2003), the relationship between the aero-dynamic diameter D_a and the maximum dimension D can be expressed as:

$$D = (34.34 D_a^{\,3})^{0.3937} \tag{3.4}$$

So assuming a bullet rosette particle habit, the cut sizes of the CVI at the airspeeds of 100 and 67 m s^{-1} are 48.3 and 58.2 microns in maximum dimension. That is to say the CVI has reduced collection efficiency (50%) of cloud droplets or ice crystals for cloud particles with a maximum dimension of about 50 microns. This reduced collection efficiency for small cloud particles of CVI may have a small effect on the IWC measurements from the CVI, which will be discussed next.

3.3 Case Study on March 9th 2000

The statistical approach discussed in section 3.1 and the in situ measurements introduced in section 3.2 are here used in the comparison of retrievals from ground-based remote sensing measurements and aircraft in situ measurements made on March 9th, 2000. The synoptic situation and aircraft flight information on that day are briefly introduced first, and then the PSD comparison and IWC comparison results are discussed.

3.3.1 Synopsis and Flight Information

On March 9th 2000, there was a southwestern jet to the west of the ARM SGP Central Facility. Heymsfield et al. (2002) gives the following information about the cirrus that developed and advected over the SGP site: “A dynamically active band of cirrus, with embedded generating cells and trails (cirrrus uncinus) moved over the operations area on March 9th 2000, producing almost exclusively single rosettes and aggregates of rosettes suitable for study.”

For the flight of the UND Citation, the following description is given by Mace et al. (2002): "The Citation began collecting data along 75 km level legs centered on the CART site near cloud top (9.4 km) at approximately 19:20 UTC. During the ensuing 90 minutes, the Citation conducted 5 level legs, stepping down through the cloud layer during the period. " The radar reflectivity and the flight path of the UND Citation on March 9th 2000 are shown in Figure 8.

3.3.2 Comparison of PSD

Using the statistical approach mention in section 3.1, the PSD retrievals from the algorithm discussed in Chapter 2 are compared with in situ measurements from the PMS 2DC and the FSSP during the first five horizontal legs of the UND Citation on March 9th, 2000. However, due to the 10-minute time resolution of the Raman lidar, there are only seven retrieval results available for comparison during the five horizontal legs, which are shown as the red X's in Figure 8. However, the second and the third PSD retrievals on the second horizontal leg show strong bimodality, and the comparisons with in situ measurements are shown in Figure 9 (a) and (b). In Figure 9, the green envelope is the uncertainty of PSD retrievals (calculated from the retrieval uncertainties of PSD parameters) estimated by the optimal estimation method from the radar and lidar measurement errors and the empirically derived model parameter errors.

Since bullet rosette is the predominant particle habit on March 9th 2000, the mass and area-dimensional parameters for five branched bullet rosettes in Mitchell (1996) are used in the algorithm. The uncertainties for these model parameters are assumed to be within 20%, and the uncertainties for Z_e, V_{dq}, β_{ext} are assumed to be 25%, 30%, and 20%,

respectively, as discussed in Chapter 2.

The blue lines in Figure 9 show all 5 seconds averaged in situ measurements selected using the statistical method discussed in section 3.1 to compare with the remote sensing retrievals. We find that for large particles, most PSD in situ measurements from the 2DC fall inside the retrieval uncertainty envelope, and the averaged PSDs agree well with the large mode PSD retrievals. However, for sub-50 micron small particles, the averaged concentration of small particles from the FSSP is about 10 times larger than that of the retrieved small mode concentration, and all in situ PSD measurements from the FSSP used in the average are outside the retrieval uncertainty envelope.

So from the above comparison of bimodal PSD retrieval and PSD in situ measurements from 2DC and FSSP, we find that the large mode PSD retrievals from the ground-based remote sensing measurements agree well with PSD from 2DC. However, the small mode PSD retrievals are not consistent with the high concentrations of small particles measured by the FSSP. The other five comparisons of PSD during the horizontal flight legs are shown in Figure 10.

In these cases, only one large mode PSD is retrieved by the algorithm from the radar and lidar measurements because, given the radar reflectivity measurements and the terminal fall velocity retrieval, the extinction calculated for the first guess is less than or equal to the extinction retrieved from the Raman lidar. Therefore, the small mode PSD is not necessary and not appropriate to be included for the optimal estimation method to retrieve the optical extinction from the Raman lidar.

For these PSD comparisons, the PSD retrievals also agree well with the averaged 2DC in situ measurements, and most 2DC in situ measurements used in the average fall inside

the uncertainty envelope of the PSD retrievals. However, the number concentrations from the FSSP are still much larger than the retrievals implying that the high concentrations of small particles measured by the FSSP are not consistent with the remote sensing measurements collected during the flight legs.

3.3.3 Comparison of IWC

As mentioned above, the CVI cannot measure cloud particles less than a certain size, so before the comparison of IWC retrieval with IWC from the CVI, this effect should be examined first.

Following the discussion above, the cut size of the CVI is about 50 microns in maximum dimension. So the IWC contribution from ice crystals with maximum dimension less than 50 microns should be examined.

Since seven PSDs during the horizontal flight legs are retrieved, the IWC from sub 50 micron ice crystals can be calculated by integrating the particle size from zero to 50 microns, and it can be written as:

$$IWC_{50} = \int_0^{50} a_m D^{b_m} N(D) dD \tag{3.5}$$

The IWC_{50}, the IWC retrievals, and the ratio of IWC_{50} to IWC retrievals for the seven comparison points are listed in Table 7. From Table 7, we see that the contribution of IWC from sub 50 micron ice crystals is generally very small. If a single mode PSD is retrieved, such as comparison point 1, 4, 5, 6 and 7, the contribution of IWC_{50} to the total IWC retrieval is below 1%. If a bimodal PSD is retrieved, such as point 2 and 3, which

the number concentrations of small particles are very large, then the ratio of IWC_{50} to total IWC is greater than 1%, but still less than 6%.

The IWC is approximately proportional to the third moment of the PSD, large particles have a much larger impact on the IWC than small particles, so it is expected that the IWC contribution from small particles should be very small. The above calculation confirms this and it also shows that if the PSD is bimodal, the IWC contribution from small particles could be larger than the small particle IWC contribution of a single mode PSD. However, the ratio of IWC_{50} to the total IWC is still very small. So in the comparison of aircraft in situ measurements with ground-based remote sensing retrievals, considering the other major error sources, the cut size effects in the CVI instruments can be neglected.

After the examination of the cut size effects of the CVI, the IWC retrieval is compared with the IWC from the CVI. The IWC retrieval can be calculated from Equation (2.21) in Chapter 2. The mean value of the IWC in situ measurements for each point during the five horizontal legs can be calculated using the statistical approach discussed above. The IWC retrieval, the mean IWC in situ data, together with their uncertainties and CVI sample quantities are listed in Table 8.

We compare the Probability Density Function (PDF) of IWC retrieval with the PDF of the IWC in situ measurements, as shown in Figure 11. Using the retrieved IWC as the mean value and the uncertainty of the IWC as the standard deviation, the PDF of the retrieved IWC is plotted as a Gaussian distribution and compared to CVI measurements in Figure 11 using the same time-space conversion approach described above.

For the first point, there are only three in situ IWC samples selected by the statistical method, and they are all close to the mean value of the retrieval. For the second point, most in situ samples fall inside the three sigma area of the Gaussian PDF of the retrieval. However, for the rest of the points, several of the in situ samples are outside the three sigma area of the retrieval PDFs. Therefore, the means of the in situ measurements do not agree well with the retrieval results, as shown in Table 8. However, for all the comparison points, the peaks of the in situ measurement PDFs are within the retrieval PDFs.

Table 6. UND Citation Instruments and measurements.

Instruments	Measurements
Forward Scatter Spectrometer Probe	Size distribution (2-47 μm)
PMS 2 Dimension Cloud Probe	Size Distribution (60-1500 μm)
Counterflow Virtual Impacter	Ice Water Content
Cloud Particle Imager	Particle images (used for particle habits)

Table 7. Percentage of IWC_{50} in the total IWC.

	IWC_{50} (g m^{-3})	IWC total (g m^{-3})	IWC_{50}/ IWC
1	$2.796e^{-5}$	$6.007e^{-3}$	0.47%
2	$11.752e^{-5}$	$2.325\ e^{-3}$	5.05%
3	$11.245e^{-5}$	$5.244\ e^{-3}$	2.14%
4	$1.386e^{-5}$	$5.641\ e^{-3}$	0.25%
5	$1.519e^{-5}$	$5.350\ e^{-3}$	0.28%
6	$1.059e^{-5}$	$2.323\ e^{-3}$	0.46%
7	$0.679e^{-5}$	$1.617\ e^{-3}$	0.42%

Table 8. The mean and standard deviation for IWC in situ data and IWC retrieval.

	In situ measurements			Retrievals	
	Mean (g/m^3)	STD (g/m^3)	Sample number	Solution (g/m^3)	Uncertainty
1	0.0044	0.0037	3	0.0060	90%
2	0.0033	0.0028	29	0.0023	80%
3	0.0119	0.0069	27	0.0052	93%
4	0.0223	0.0129	17	0.0056	90%
5	0.0113	0.0093	29	0.0054	90%
6	0.0083	0.0068	24	0.0023	88%
7	0.0073	0.0079	38	0.0016	56%

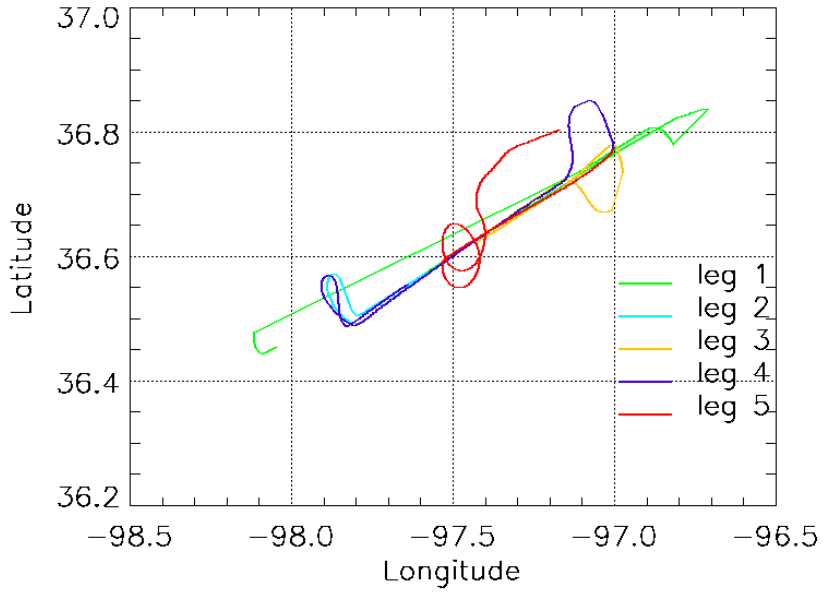

Figure 7. Coordinates of the airplane positions during the first five legs.

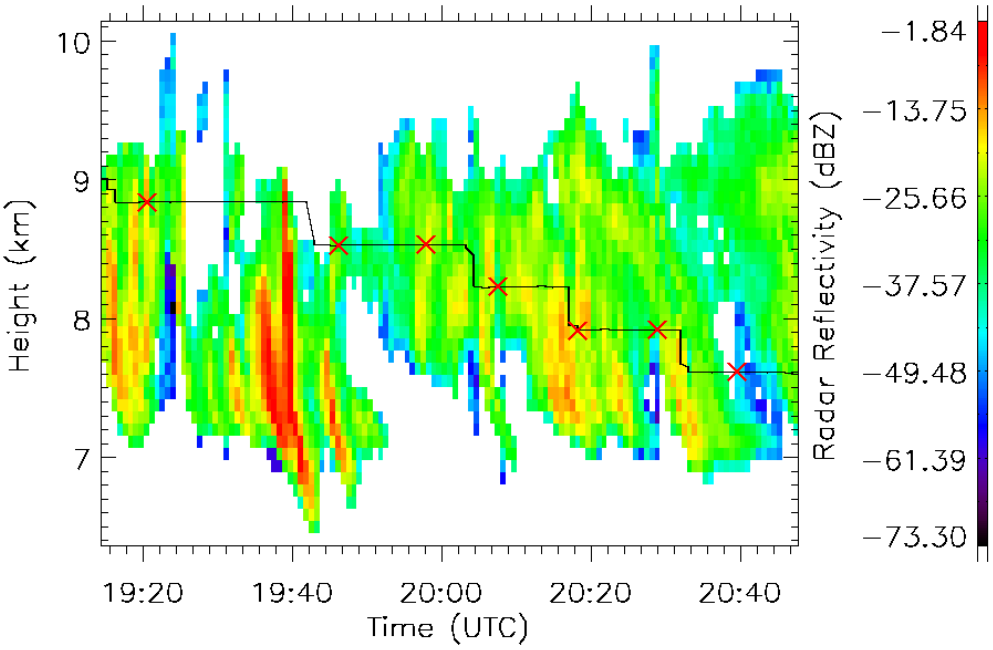

Figure 8. Flight path and radar reflectivity cross section on March 9th 2000.

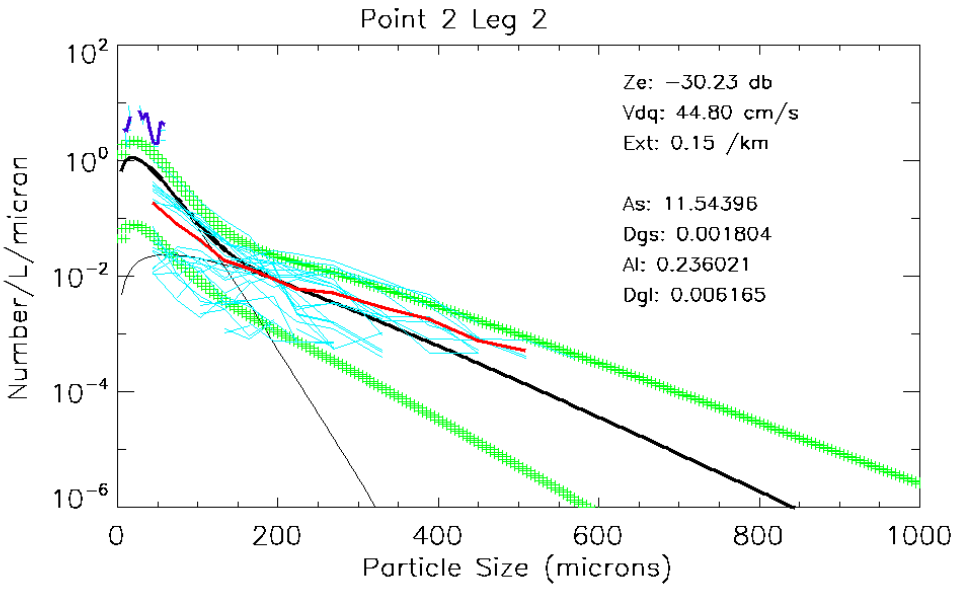

(a) PSD retrieval at the second point during leg 2

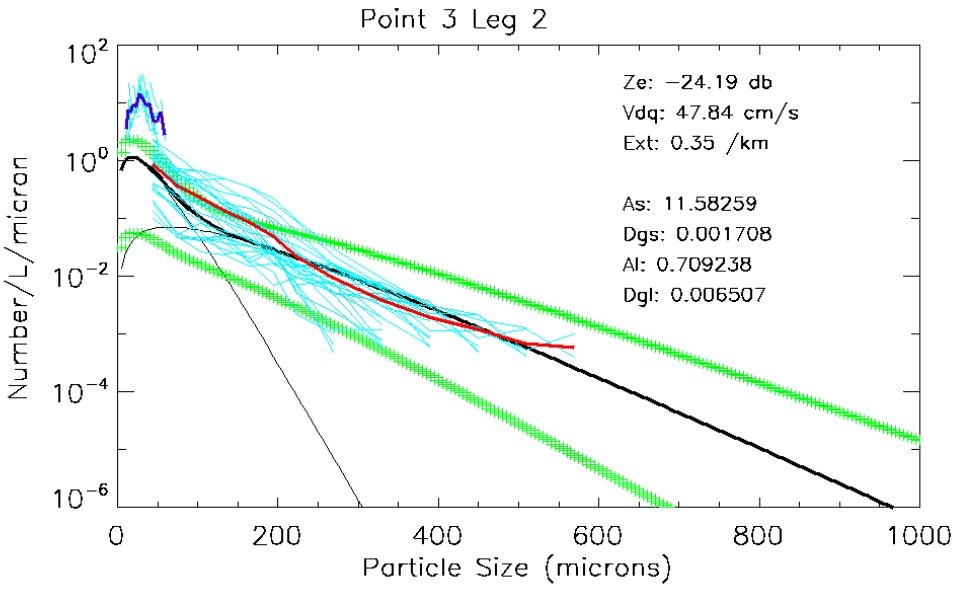

(b) PSD retrieval at the third point during leg 2

Figure 9. Comparisons of PSD retrievals and PSD in situ measurements.

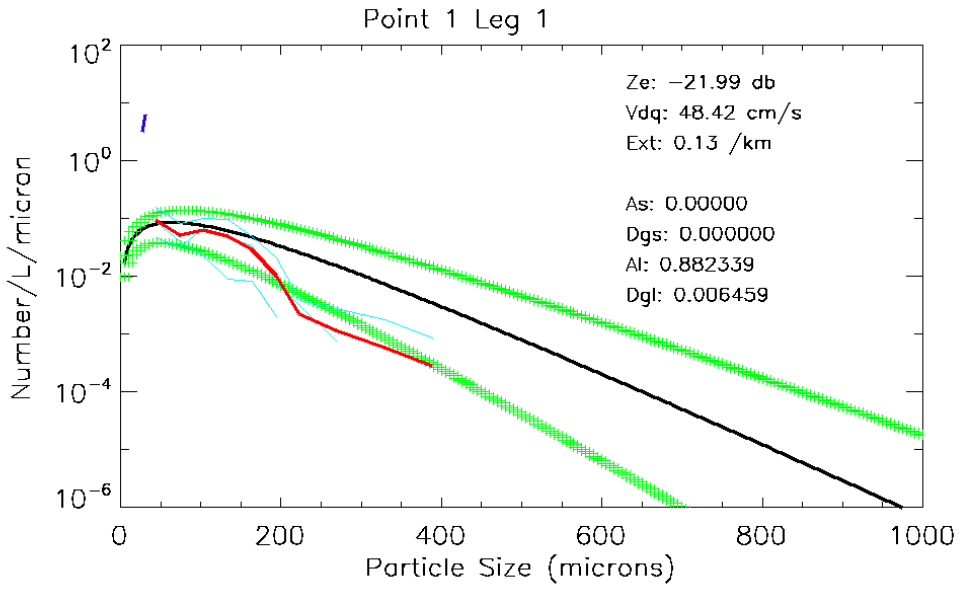

(a) Point 1

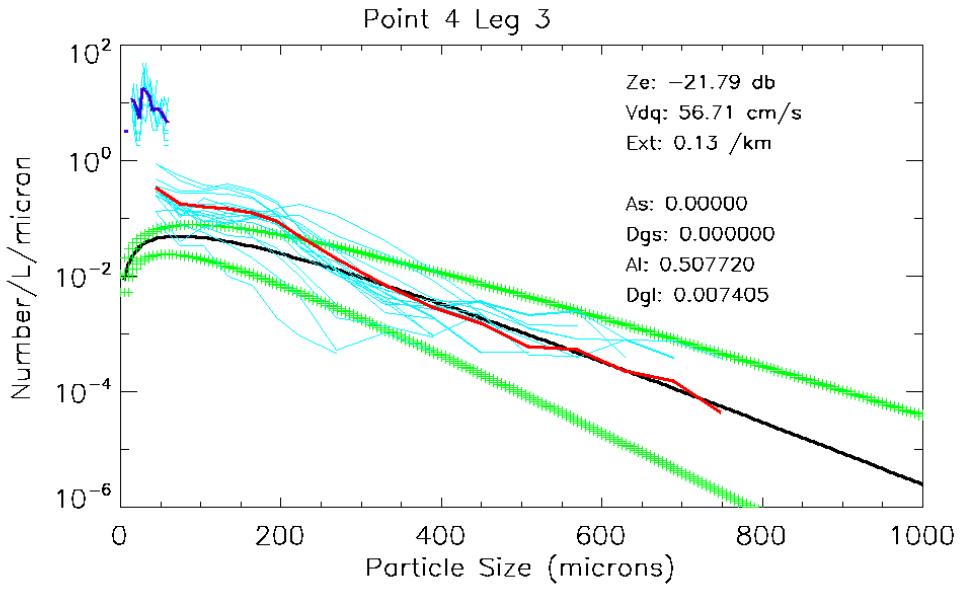

(b) Point 4

Figure 10. Comparisons of single mode PSD retrievals with in situ data.
(Point 1: (a); Point 4: (b); Point 5: (c); Point 6: (d); Point 7: (e))

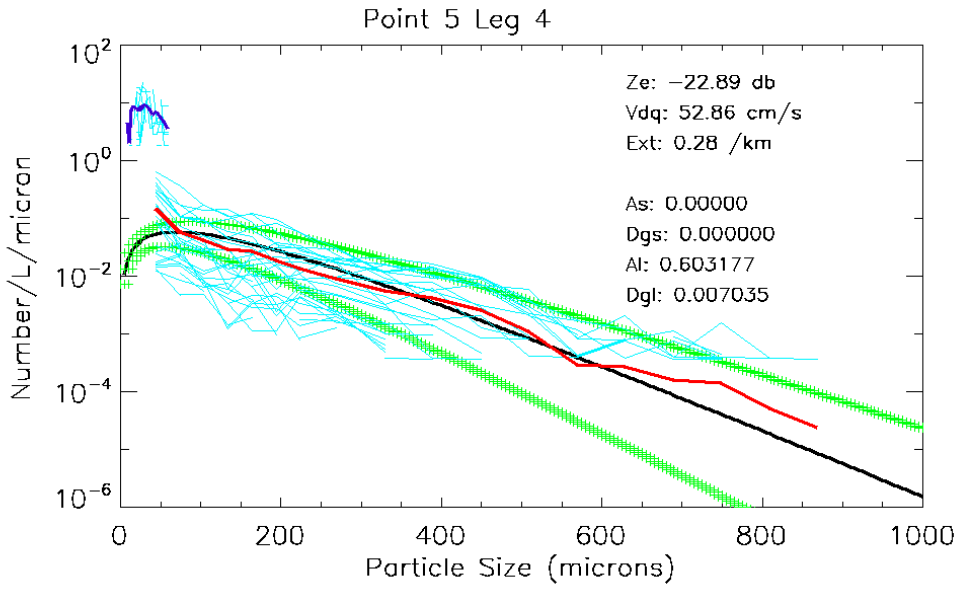

(c) Point 5

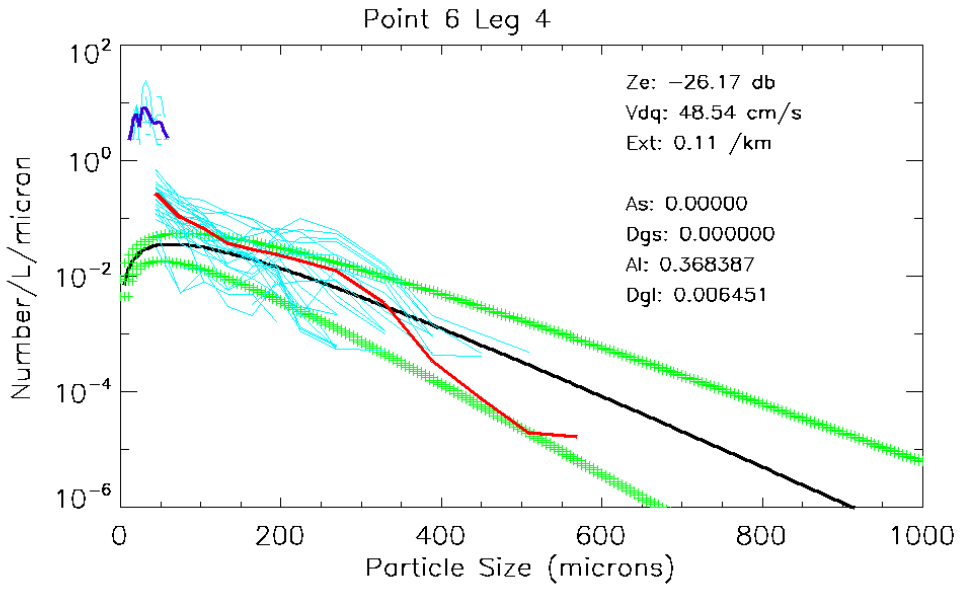

(d) Point 6

Figure 10. continued.

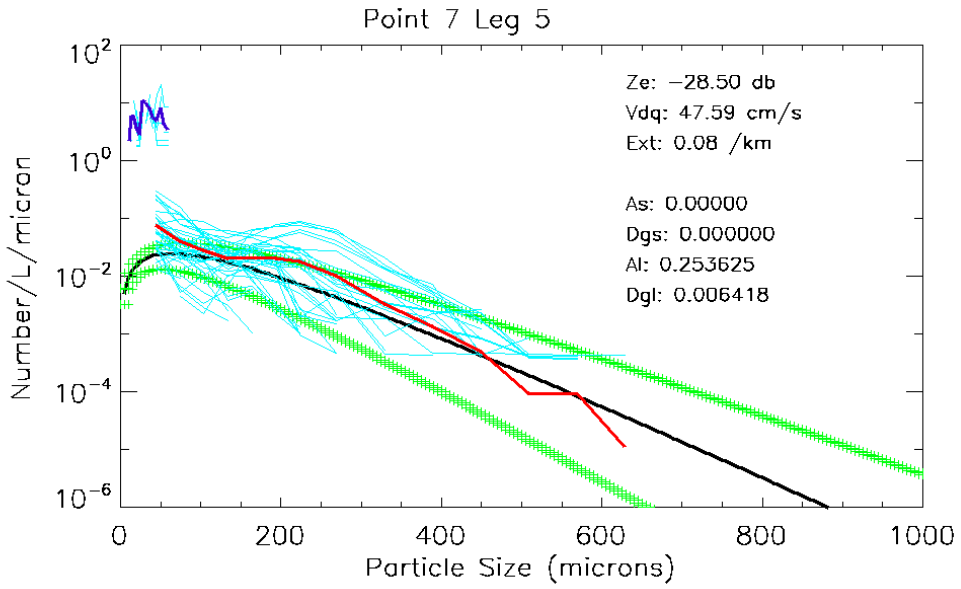

(e) Point 7

Figure 10. continued.

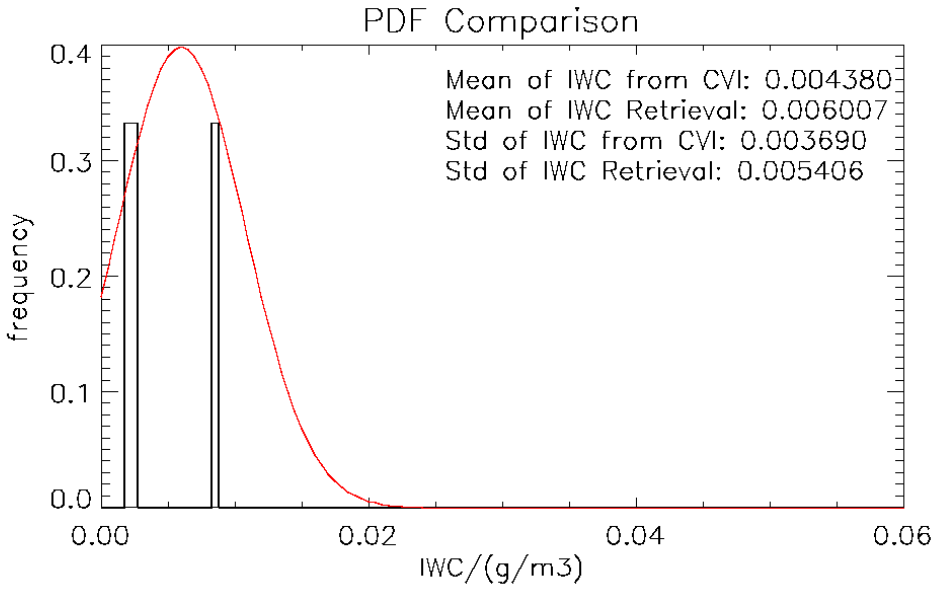

(a) Point 1

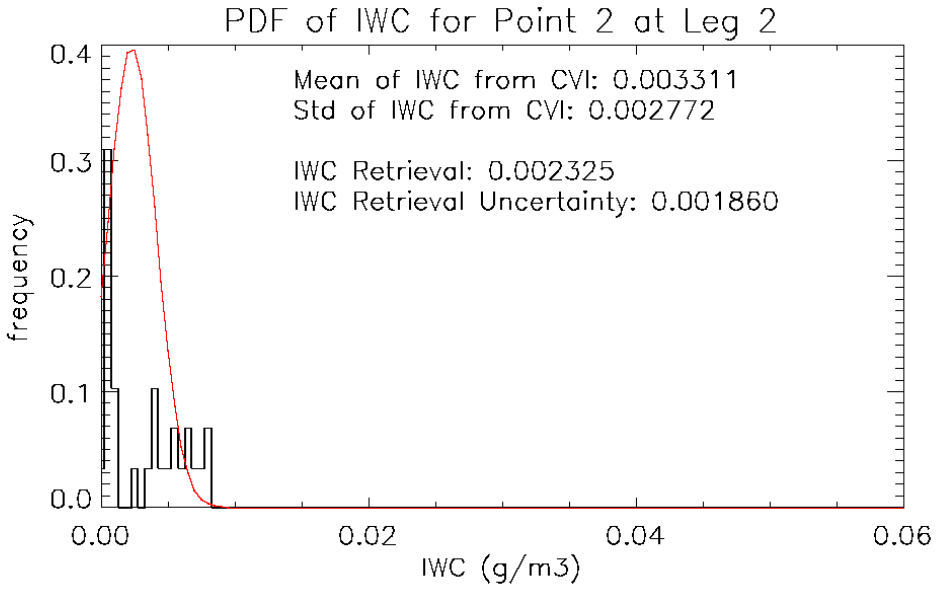

(b) Point 2

Figure 11. PDF of retrievals and in situ data.
(Point 1: (a); Point 2: (b); Point 3: (c); Point 4: (d); Point 5: (e); Point 6: (f); Point 7: (g))

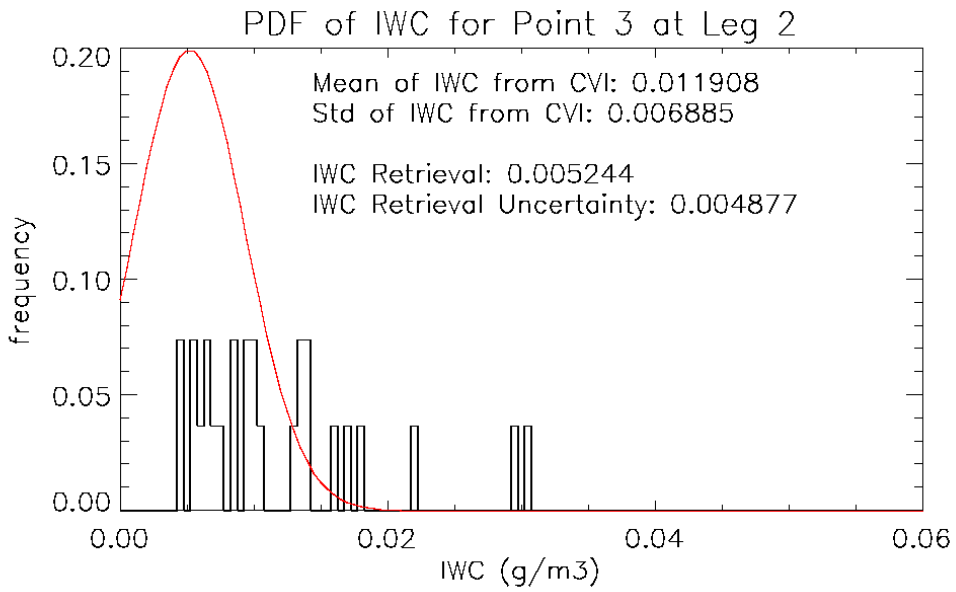

(c) Point 3

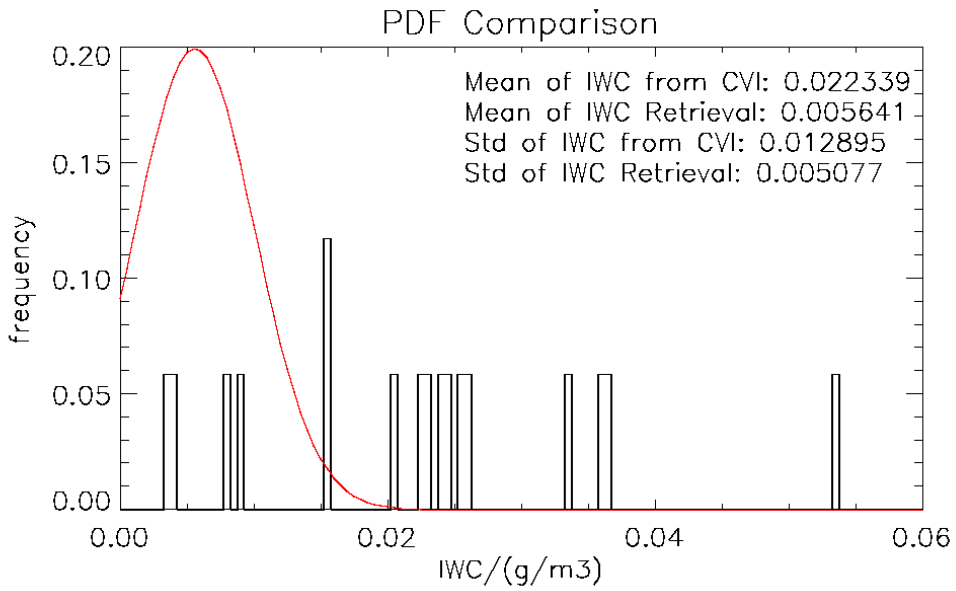

(d) Point 4

Figure 11. Continued.

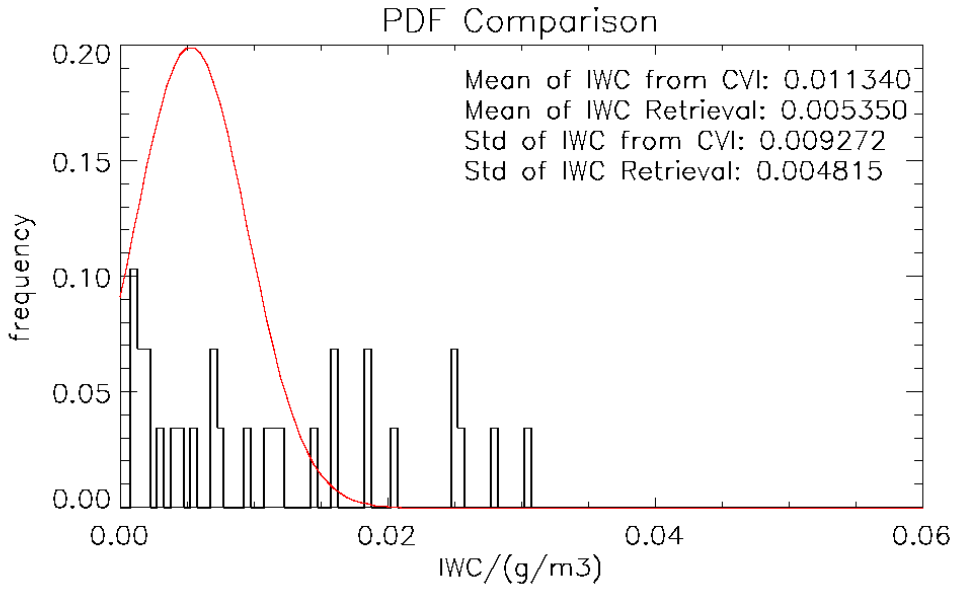

(e) Point 5

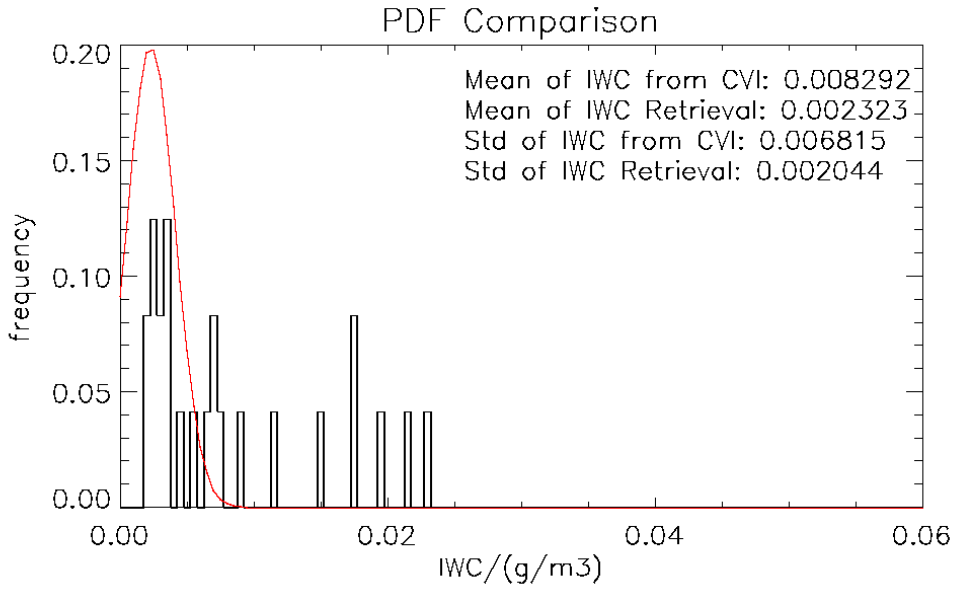

(f) Point 6

Figure 11. Continued.

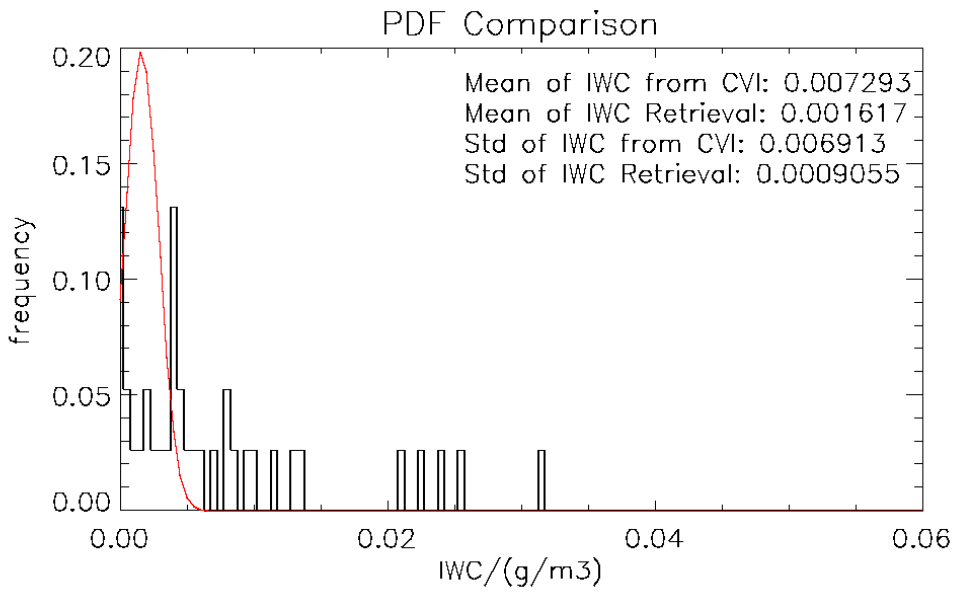

(g) Point 7

Figure 11. Continued.

CHAPTER 4

ONE-YEAR STATISTICS

Many recent studies using aircraft in situ measurements (e.g., Lawson et al., 2006) show that the average particle concentrations in midlatitude cirrus clouds are on the order of 1 cm^{-3}. However, other studies (Heymsfield, 2007; McFarquhar et al., 2007) suggest that the cirrus microphysical statistics derived from aircraft in situ measurements may be biased due to an artificial enhancement in small ice crystals from the shattering of larger ice crystals on aircraft and probe surfaces. To see if the cirrus statistics from aircraft in situ measurements are consistent with that from remote sensing retrievals, appropriately formulated retrieval algorithms need to be applied to long-term remote sensing measurements. The cirrus statistics from long-term remote sensing retrievals have been derived by only a few studies (Mace et al., 2006; Deng and Mace 2008). However, the algorithms used in those studies were not capable of retrieving high concentrations of small crystals because of an assumption of a single mode PSD. An algorithm that is capable of retrieving a bimodal PSD similar to what is typically seen in aircraft data, and thus can represent microphysical properties for both small particles and large particles, has never been applied to long-term ground-based remote sensing measurements. In this chapter, the algorithm described in Chapter 2 is applied to 313-hour cirrus events observed at the ARM SGP site, and 33641 retrievals are used to study cirrus microphysical statistics.

4.1 PSD Bimodality Statistics

The existence of bimodality indicates certain microphysical processes, such as secondary nucleation of ice crystals within a cirrus layer (Comstock et al., 2008). The presence of significant bimodality also has implications for cirrus cloud property retrievals from ground-based and space-based sensors. We emphasize the word "significant" because quite often the algorithm used in this study diagnoses a PSD that utilizes both gamma functions to best represent the data. However, quite often a unimodal description of the PSD would be sufficient to describe, to within some specified degree of uncertainty, the PSD moments that are most relevant to the integrated physical quantities such as IWC, effective radius, and extinction. Previous studies, such as Mace et al. (2002), used aircraft in situ data to study the frequency of occurrence of bimodal size distributions in cirrus. However, an examination of bimodality has never been applied to long-term remote sensing measurements.

The approach that we take is to fit the retrieved PSD using unimodal distribution functions and then to use the misfit between the PSD retrieval and the fitted PSD to ascertain the degree of bimodality of the PSD. A modified gamma function with three degrees of freedom is used as the fitting function. The difference of the second, third and fifth moments of the retrieved PSD and the fitted gamma function is used as the cost function, which is written in Equation (4.1).

$$f = \sqrt{\left|\frac{\mu_2' - \mu_2}{\mu_2}\right|^2 + \left|\frac{\mu_3' - \mu_3}{\mu_3}\right|^2 + \left|\frac{\mu_5' - \mu_5}{\mu_5}\right|^2} \tag{4.1}$$

where μ_2', μ_3', μ_5' are the second moment, the third moment and the fifth moment of the fitted PSD, respectively, and μ_2, μ_3, μ_5 are the second moment, the third moment and the fifth moment of the PSD retrieval.

Because the second, third and fifth moment approximately correspond to the extinction, the IWC and the radar reflectivity, respectively, the difference between the PSD retrieval and the unimodal PSD function can be measured by these quantities with actual physical meanings. Once the fitting function and the cost function are chosen, the amoeba algorithm, which is a commonly used nonlinear optimization algorithm (Nelder and Mead, 1965), is used in the minimization. The misfit between the fitted PSD and the PSD retrieval can be calculated from the cost function expressed in Equation (4.1).

Finally, a threshold value for the misfit needs to be set to distinguish a strong bimodal PSD retrieval from a single mode PSD retrieval or a weak bimodal PSD retrieval. Many PSD retrievals have been investigated to find a proper threshold for strong bimodal PSD, and four examples are shown in Figure 12. In the first PSD example shown in Figure 12 (a), the magnitude of the small mode PSD is very small. The misfit between the gamma function fit and the bimodal PSD is only 1%. The misfit of the second PSD example increases to 10%, the bimodality also increases, but it is still a weak bimodal PSD. In Figure 12 (c) and Figure 12 (d), the PSD retrievals show stronger bimodality. One gamma function cannot represent the bimodal PSD, and the misfits are 20% and 30%, respectively. From the above and other examples that we have studied, 30% is chosen to be a proper threshold to distinguish a strong bimodal PSD from a unimodal PSD or a weak bimodal PSD. This value of misfit is approximately the degree of uncertainty that one would expect in retrieving the PSD moments from either remote sensing data or from

in situ data and so is an appropriate threshold metric for our purposes.

After defining a proper and physically meaningful way to measure PSD bimodality, the variation of the PSD bimodality with the environmental temperature and radar reflectivity is explored by using 33641 ground-based remote sensing retrievals.

The histogram of the bimodality frequency in terms of radar reflectivity and temperature is shown in Figure 13. The bimodality frequencies for cirrus with very small radar reflectivities (less than -35 dBZ) at very low temperatures (lower than 230 K) are generally below 25%. As the temperature increases, the bimodality frequency also increases. However, when radar reflectivity is above -15 dBZ, the bimodality frequency is generally less than 20%, regardless of the temperature. A bimodality occurrence frequency of more than 40% only happens when the temperature is above 240K and radar reflectivity is below -15 dBZ. If the temperature is below 240K, the bimodality frequency is generally less than 30%. The bimodality frequency histogram shows a dependency of PSD bimodality on temperature when the radar reflectivity is less than -15 dBZ, and this dependency is shown again in the bimodality frequency vertical profile in Figure 14. In Figure 14, the bimodality frequency profiles are plotted separately for cirrus with different temperature ranges. Cirrus with temperature less than 223K (coldest cirrus) is shown in black, cirrus with temperature between 223K and 243K is in green, and the warmest cirrus with temperature higher than 243K is shown in red.

For the coldest cirrus, the bimodality frequencies are all below 20%, and the profile does not change much from the cloud bottom, where the normalized height (Mace et al., 1997) is zero, to the cloud top, where the normalized height is unity. However, for the warmest cirrus, the bimodality frequency drops rapidly from more than 40% at the cloud

top to less than 20% in the lower half of the profile, and then increases to about 40% near the cloud base. The decrease in the bimodality frequency for the warmest cirrus in the upper half of the profile may be related to the heterogeneous nucleation of new ice crystals as larger crystals sediment through the layer. Small ice crystals and middle-sized ice crystals at the cloud top tend to form larger-sized ice crystals, which would dominate the total population of the ice crystals.

4.2 PDFs of IWC, Effective Radius and Concentration

4.2.1 PDF of IWC

The PDFs of the IWC retrieval, shown in Figure 15, demonstrate a clear dependence on temperature (e.g., Heymsfield and Platt, 1984) in their mean, mode, and variance.

The coldest third of cirrus (T < 223K; hereafter coldest cirrus) has the lowest IWC mean value, about 1.61 mg m^{-3} with a standard deviation (STD) of 2.69 mg m^{-3} The warmest third of cirrus (T > 243K; hereafter warmest cirrus) has the highest mean value, which is 12.60 mg $m^{-3}$with a standard deviation of 17.07 mg m^{-3}. The middle-temperature cirrus (223K < T < 243K) has a mean IWC of 6.09 mg m^{-3} (standard deviation of 10.56 mg m^{-3}), which is in the middle of the mean IWC of the warmest cirrus and the coldest cirrus. Consistent with the mean value, the PDF of the coldest cirrus is the narrowest, extending from 0.1 mg m^{-3} to about one mg m^{-3}; but for the warmest cirrus, the PDF extends across the entire range from 0.1 mg m^{-3} to hundreds of mg m^{-3}.

The modal values of IWC also increase substantially with temperature. The coldest cirrus has a very large and narrow maximum with a peak frequency of almost 25%, which means that almost 25% of IWC that the coldest cirrus has is among the range of

1.25 to 2.0 mg m^{-3}. For the middle-temperature cirrus, it has a relatively lower maximum (about 17%) at a larger IWC (about 8.0 mg m^{-3}), and for the warmest cloud, the PDF is flat and ranges between 1.25 to 31.6 mg m^{-3}.

From the above comparisons of the IWC PDF of three types of cirrus, we can clearly see the difference in these three different cirrus types in terms of the mean, mode and variance. The warmest cirrus has the largest mean IWC, the widest PDF width and the lowest PDF peak, while the coldest cirrus has the lowest mean IWC, the narrowest PDF width and the highest PDF peak at the lowest IWC value.

4.2.2 PDF of Effective Radius

To provide convenience for climate modeling, the statistics of the effective radius instead of the mass mean size are also derived from remote sensing retrievals. The PDF of the effective radius also demonstrates a strong dependence on temperature with highly skewed distribution.

One significant feature of the effective radius PDF shown in Figure 16 is the high peak at about 10 microns for the PDF of the coldest cirrus. Its PDF reaches a maximum of about 35%, which is more than twice of the maximum of the warmest and middle-temperature cirrus PDFs, and then it quickly decreases to a frequency near zero at 30 microns. More than 80% of the PDF area falls below 20 microns, which suggests that for the coldest cirrus, most effective radii are below 20 microns. However, for the middle-temperature cirrus and the warmest cirrus, their effective radius PDF maxima are smaller, but they both have a much wider PDF width, extending from 5 microns to more than 70 microns. More than 50% of the PDF area is above 20 microns for both the warmest cirrus

and the middle-temperature cirrus. With regard to the mean value, the coldest cirrus has the smallest mean effective radius, about 12 microns with a standard deviation of 6.9 microns; the warmest cirrus has the largest mean value, about 31 microns with a standard deviation of about 21 microns; and the mean effective radius for the middle-temperature cirrus is in the middle, about 23 microns with a standard deviation of 14 microns. The mean values of the effective radius retrievals are generally smaller than those of previous studies (Wang and Sassen, 2001). However, they are consistent with the results reported in Donovan (2003), which also uses a bimodal PSD assumption.

4.2.3 PDF of Concentration

The PDFs of the number concentration retrieval for cirrus with different temperatures are shown in Figure 17. The PDF of the coldest cirrus also shows a very different feature compared to the warmest and the middle-temperature cirrus in terms of mean value and mode. The mean concentration for the coldest cirrus is about 101 l^{-1} with a standard deviation of 276.5 l^{-1}, while for the middle-temperature cirrus and the warmest cirrus, they are 58 (standard deviation of 167.8 l^{-1}) and 40 l^{-1} (standard deviation of 211.8 l^{-1}), respectively. The coldest cirrus has a much larger mean concentration than that of the others. In terms of PDF mode, the PDF of the coldest cirrus is the narrowest, 80% of its area is from about 10 l^{-1} to 400 l^{-1}. For the warmest and the middle-temperature cirrus, their PDF widths are wider, and more PDF area is in the region of 1 l^{-1} to 10 l^{-1}. However, for all cirrus, the occurrence frequencies of the total number concentrations larger than 1000 l^{-1} (1 cm^{-3}) are below 1%. So the remote sensing retrievals suggest that it is very rare to have a total number concentration larger than 1000 l^{-1} in cirrus. This result is totally inconsistent with the conclusions drawn from many studies that relied on in situ

measurements that were not carefully filtered for shattering artifacts. These studies claim that the average particle concentration in midlatitude cirrus is on the order of 1 cm^{-3} (Lawson et al., 2006). The presence of shattering artifacts may be the prime reason for this large discrepancy. However, we can conclusively state that such average concentrations as derived from aircraft data are entirely inconsistent with any reasonable interpretation of the Raman lidar and Doppler Radar data collected at the ARM SGP site.

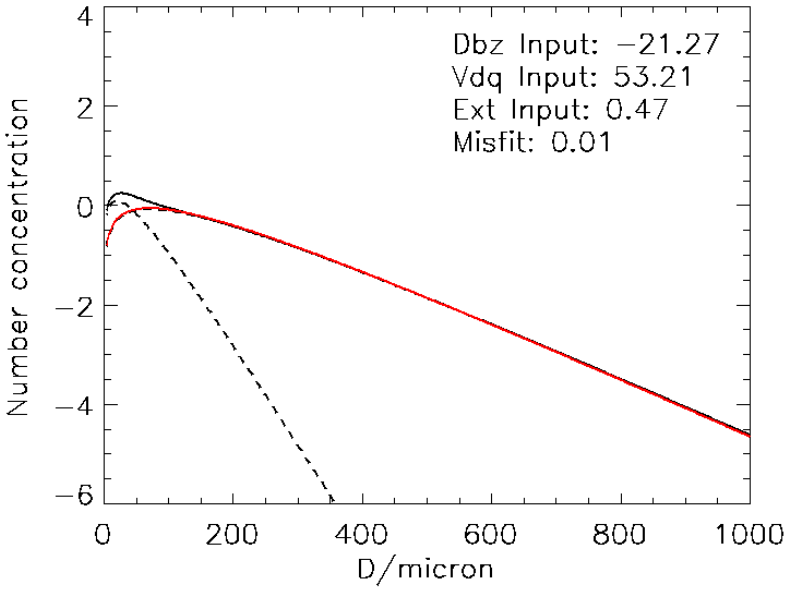

(a) Misfit=1%

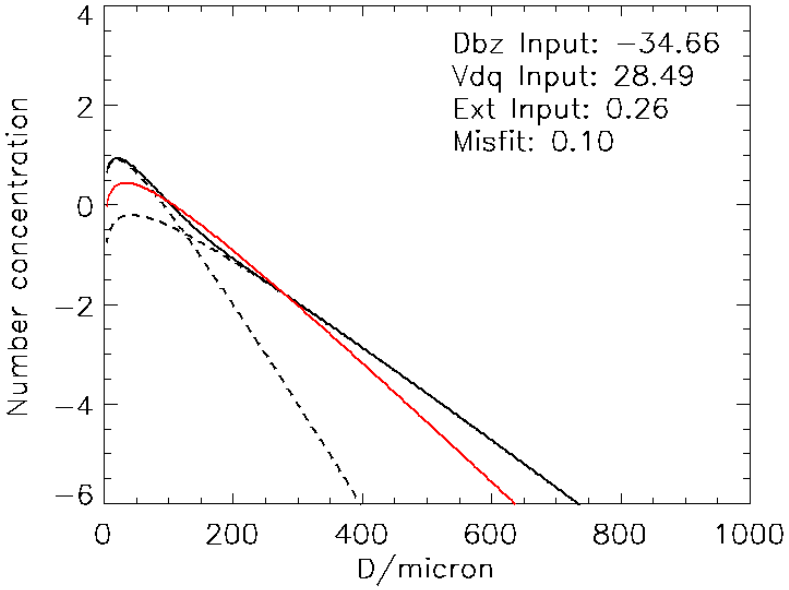

(b) Misfit=10%

Figure 12. PSD retrieval and PSD fit with different misfits. (Black solid: PSD retrieval; Red solid: PSD fit; Black dash: Large and small mode retrievals)

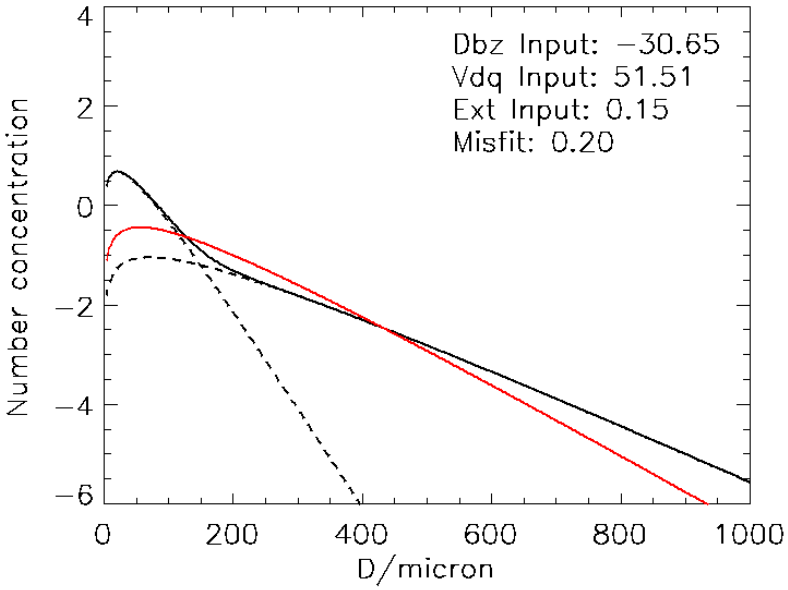

(c) Misfit=20%

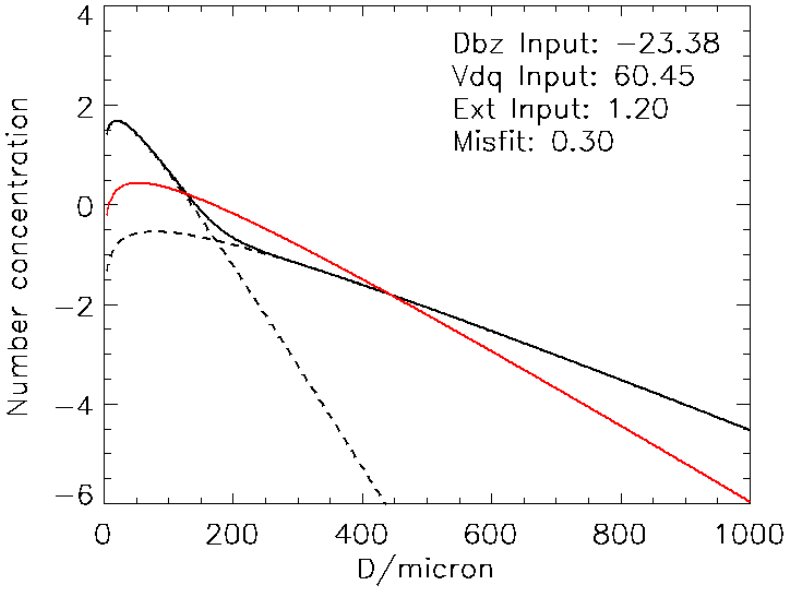

(d) Misfit=30%

Figure 12. continued.

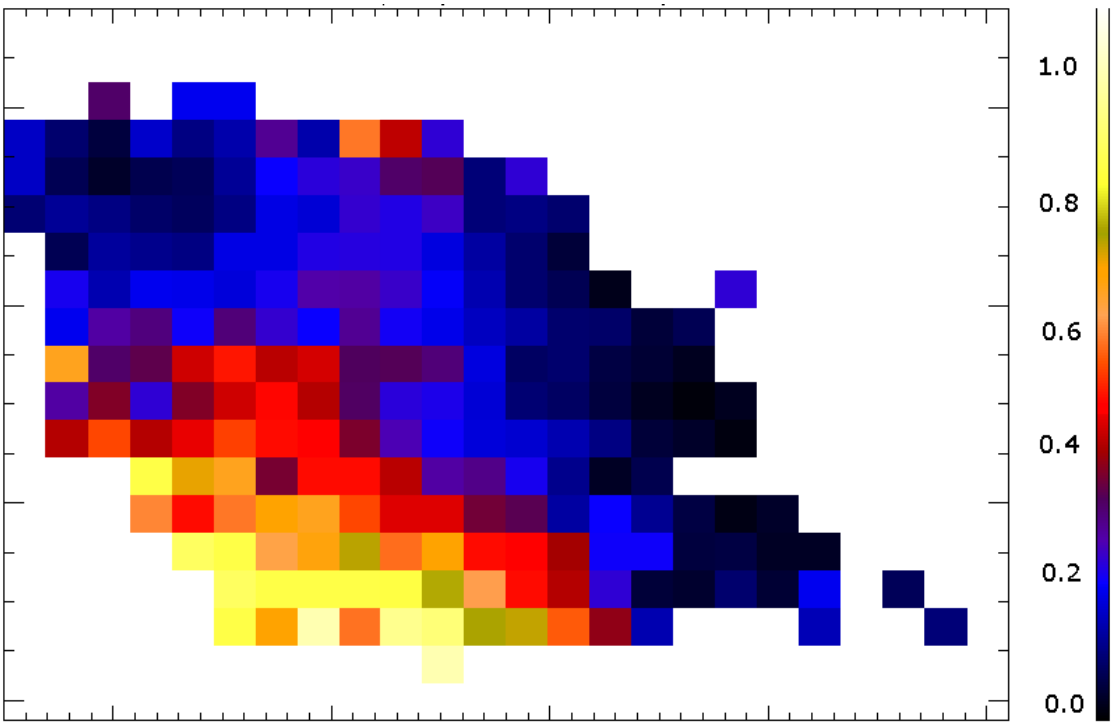

Figure 13. Bimodality frequency histogram in terms of reflectivity and temperature.

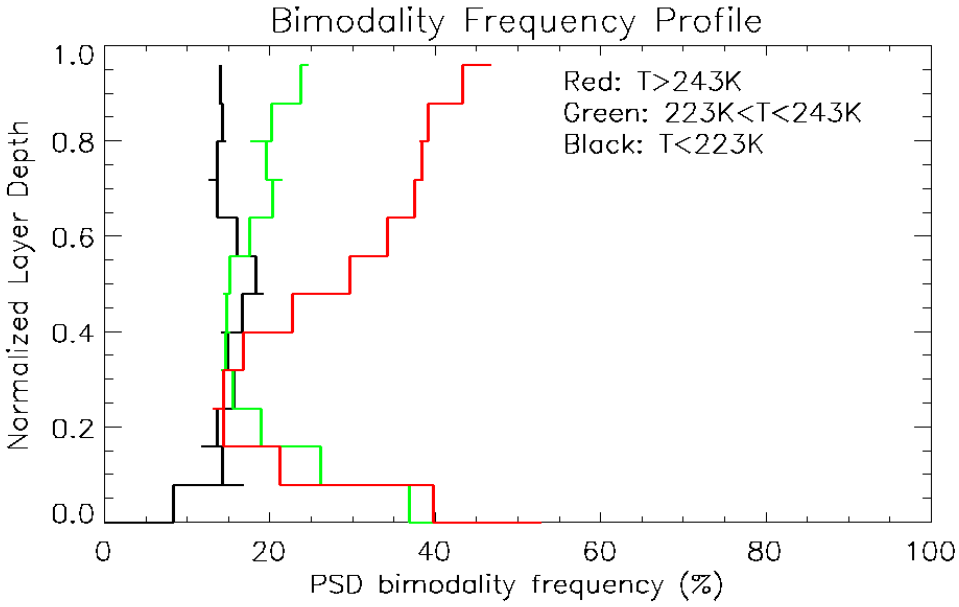

Figure 14. Bimodality vertical profiles for cirrus with different temperatures.

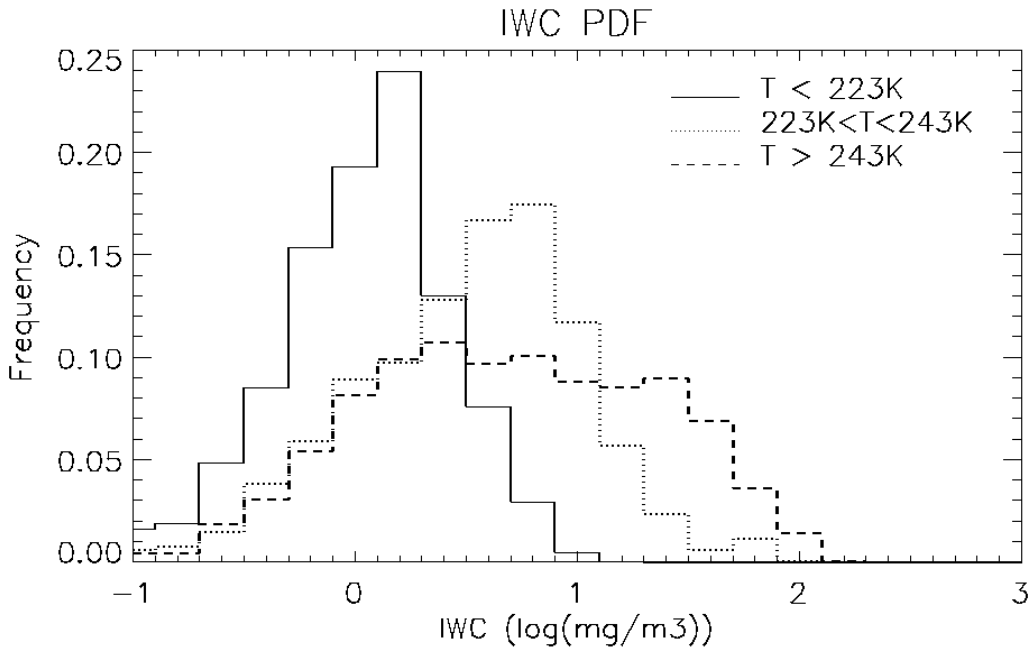

Figure 15. PDF of IWC from retrievals.

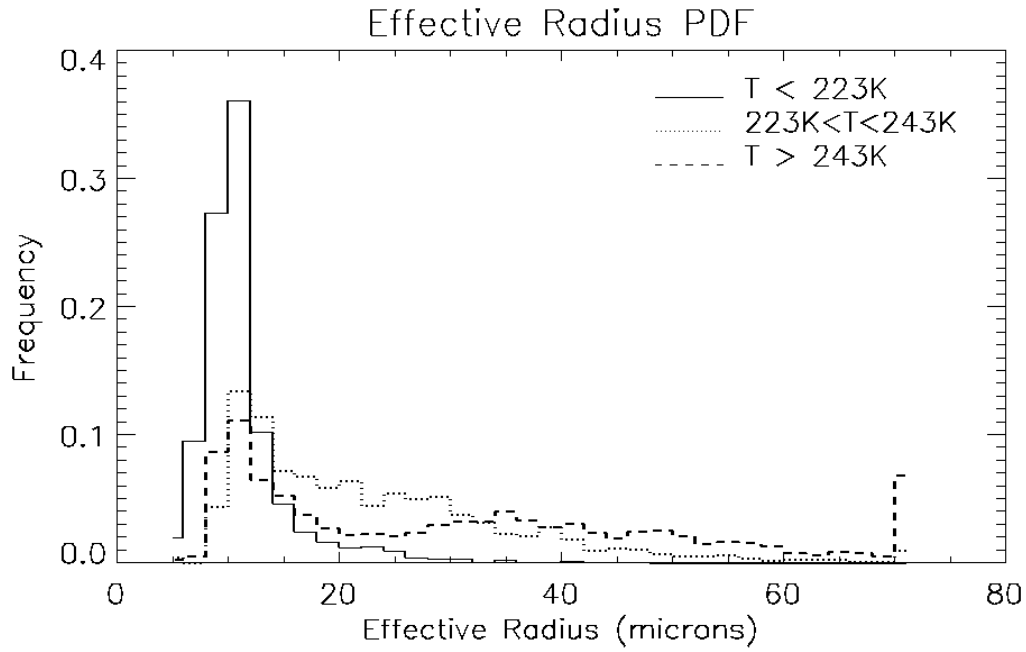

Figure 16. PDF of effective radius from retrievals.

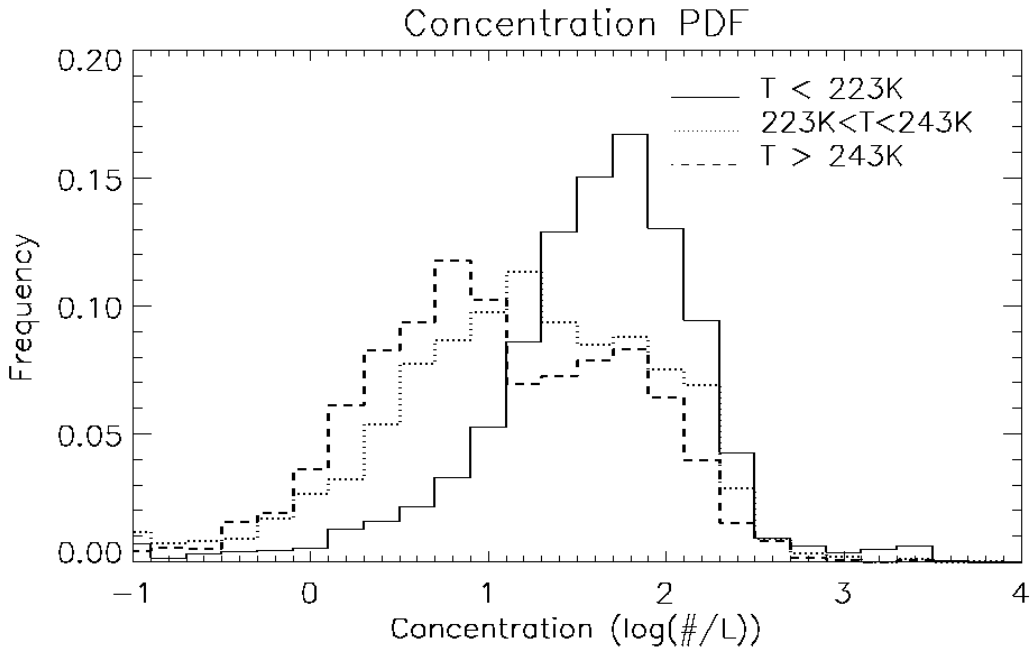

Figure 17. PDF of concentration from retrievals.

CHAPTER 5

SUMMARY

To better understand the feedback by cirrus clouds on the climate system, both the macrophysical and microphysical properties of cirrus must be quantified. At the microphysical level, how light is scattered by ice crystals, especially small ice crystals, is critically important to the solar radiative properties of the cirrus cloud. So to better quantify the scattering effects of ice crystals, many field experiments have been conducted and many in situ measurements have been made. Recent studies suggest that some aircraft in situ measurements, such as measurements from the FSSP, may be contaminated by ice crystal shattering on probe inlets and aircraft surfaces. The potential for shattering artifacts has called into question the validity of the aircraft data.

The motivation for this study is to see if the aircraft in situ measurements are consistent with ground-based remote sensing measurements. The aircraft in situ data used in this study is from the 2000 Spring Cloud IOP, and the data include the particle images from the CPI, the IWC from the CVI, and the number concentration measurements for small particles from the FSSP and those for large particles from the 2DC. The remote sensing data used in the retrieval algorithm includes the optical extinction estimation from the Raman lidar, the radar reflectivity from 35 GHz radar and the particle terminal fall velocity retrieval from an algorithm described in Deng and Mace (2006). The approach used in the study is to interpret the remote sensing data in a way that would

allow for the presence of or the absence of high concentrations of small particles. And then no matter which possibility is correct, the finding of frequent high concentrations of small particles should be consistent with remote sensing measurements. So in order to ascertain the role of small particles in actual cirrus microphysical properties, an algorithm is developed to retrieve a bimodal size distribution based on measurements from Raman lidar and Doppler radar. An assumption of bimodality in the retrieved particle size distribution would reasonably represent size distributions similar to what is typically found in in situ data if the remote sensing data suggest its presence. Because lidar measurements are more sensitive to small particles and radar measurements are more sensitive to large particles in cirrus, the retrieval algorithm is capable of retrieving a small mode and a large mode of the particle size distribution. Specifically, two modified gamma functions are used to approximate these two modes, and then based on forward model equations from radar reflectivity, Doppler velocity and lidar extinction, an inversion method is applied to get the optimal solutions and the uncertainties of the solutions. After that, the aircraft in situ measurements are compared with the remote sensing retrievals to see if they are consistent with each other. Finally, statistics from long-term retrievals are used to further ascertain the validity of the frequently observed high concentration of small particles in cirrus.

Specifically, in Chapter 2 four forward model equations are formulated to relate the radar and lidar measurements to four PSD parameters. Then an inversion technique is developed by using the Maximum A Posteriori (MAP) criterion, the Gaussian PDF assumption and the Gauss Newton numerical method. After that, the inversion technique is used in the retrieval algorithm to get both the optimal solutions of the PSD parameters

and their uncertainties. For the optimal solutions, the algorithm's ability to reach an optimal estimation of the PSD parameters is tested, and it is shown that the first guesses of the PSD parameters should be carefully chosen because of the nonlinearity of this inverse problem. For the uncertainty estimation, all possible sources of estimation error are examined, and the two biggest error sources, the model parameter error and the measurement error, are quantified by using the inversion technique. A sensitivity study is performed to show the sensitivity of the retrieval error to the model parameter error and the measurement error, and it is shown that the retrieval error is more sensitive to the empirically derived power law model parameter error than to the measurement error.

In Chapter 3, a statistical method is first introduced to minimize the time and spatial differences in the aircraft in situ measurements and the ground-based remote sensing measurements. And then the in situ measurements, including the PSD data and the IWC data from 2000 Spring cloud IOP, are used to compare with the retrieval results from Doppler radar and Raman lidar data. The PSD in situ data from the 2DC for large particles agree well with that of the retrieval results, but for small particles, the number concentrations from the FSSP are much higher (by approximately a factor of 10) than that of the retrievals, and also lie well beyond the retrieval uncertainties. The effect of ice crystal shattering on the FSSP measurements is considered as a possible reason for this inconsistency with the remote sensing retrievals.

Finally the bimodality statistics and the statistics of cirrus cloud microphysical properties are derived by applying the retrieval algorithm to long-term cirrus events. The data set used amounts to 313 hours of cirrus events collected over the SGP site during 2000. The PDFs of the IWC, the effective radius, and the number concentration are

examined for cirrus with different temperatures. We find that bimodality in the PSD is a significant feature of many cirrus particle size distributions. This is especially true at warmer cirrus temperatures in the upper half of the cirrus layer where new nucleation events occur in the presence of larger particles sedimenting from high levels. The bimodality of the particle size distribution is often prominent enough that an assumption of a single mode distribution function in remote sensing retrievals would be unable to simultaneously represent the number concentration, extinction, and IWC. Importantly, we find unequivocally that the occurrence frequencies of the total number concentrations larger than 1 cm^{-3} are less than 1% of all size distributions examined.

In sum, in this study a retrieval algorithm that is designed to retrieve high concentrations of small particles is developed. The biggest sources of retrieval error are found and quantified. The small mode concentration retrievals from ground-based radar and lidar measurements are much lower than those from the aircraft in situ measurements from the FSSP. Statistics from long-term remote sensing retrievals show that concentrations in excess of 1 cm^{-3} are extraordinarily rare, which is also inconsistent with the frequently observed high concentrations of small particles from aircraft in situ data. The presence of shattering artifacts in the aircraft in situ data may be the prime reason for the high concentrations of small particles from in situ data. However, the conclusion of this study is that high concentrations of small particles from aircraft data (about 1 cm^{-3} and larger) are inconsistent with any reasonable interpretation of the Doppler radar and Raman lidar data collected at the SGP site. So it is suggested that previous conclusions drawn from aircraft in situ data that were not carefully filtered for shattering artifacts need to be reconsidered.

APPENDIX A

SINGLE MODE RETRIEVAL ALGORITHM

If calculated lidar extinction from large mode PSD is greater than the total extinction from Raman lidar, it suggests another small mode PSD is not necessary, and in this case, an algorithm that uses radar reflectivity, Doppler velocity and lidar extinction is performed to retrieve one single mode PSD.

In this single mode radar-lidar algorithm, one modified gamma function, which is expressed in Equation (A1), is used to represent the PSD.

$$N(D) = A(\frac{D}{D_g})^{\alpha} \exp(-\frac{D - D_g}{D_g}) \tag{A1}$$

The three parameters of the gamma function are included in the vector ***x***:

$$\mathbf{x} = [A, D_g, \alpha] \tag{A2}$$

The measurements are included in the vector ***d***:

$$\mathbf{d} = [Z_e, V_{dq}, \beta_{ext}] \tag{A3}$$

The empirically derived model parameters are included in the vector ***m***:

$$\mathbf{m} = [a_m, b_m, a_a, b_a] \tag{A4}$$

Using the same assumptions in the bimodal PSD algorithm, the forward model equations are expressed in the following:

$$Z_e = Aea_z D_g^{\,b_z+7}\Gamma(\alpha + b_z + 7) \tag{A5}$$

$$V_{dq} = a_v D_g^{\,b_v} \frac{\Gamma(\alpha + b_z + b_v + 7)}{\Gamma(\alpha + b_z + 7)} \tag{A6}$$

$$\beta_{ext} = 2Aea_a D_g^{\,b_a+1}\Gamma(\alpha + b_a + 1) \tag{A7}$$

The Jacobian matrices that represent the sensitivity to the vector ***x*** and the vector ***m*** are expressed in Equation (A8) and (A9).

$$\mathbf{K_x} = \frac{\partial \mathbf{F}}{\partial \mathbf{x}} = \begin{bmatrix} \frac{\partial Z_e}{\partial A} & \frac{\partial Z_e}{\partial D_g} & \frac{\partial Z_e}{\partial \alpha} \\ \frac{\partial V_{dq}}{\partial A} & \frac{\partial V_{dq}}{\partial D_g} & \frac{\partial V_{dq}}{\partial \alpha} \\ \frac{\partial \beta_{ext}}{\partial A} & \frac{\partial \beta_{ext}}{\partial D_g} & \frac{\partial \beta_{ext}}{\partial \alpha} \end{bmatrix} \tag{A8}$$

$$\mathbf{K_m} = \frac{\partial \mathbf{F}}{\partial \mathbf{m}} = \begin{bmatrix} \frac{\partial Z_e}{\partial a_m} & \frac{\partial Z_e}{\partial b_m} & \frac{\partial Z_e}{\partial a_a} & \frac{\partial Z_e}{\partial b_a} \\ \frac{\partial V_{dq}}{\partial a_m} & \frac{\partial V_{dq}}{\partial b_m} & \frac{\partial V_{dq}}{\partial a_a} & \frac{\partial V_{dq}}{\partial b_a} \\ \frac{\partial \beta_{ext}}{\partial a_m} & \frac{\partial \beta_{ext}}{\partial b_m} & \frac{\partial \beta_{ext}}{\partial a_a} & \frac{\partial \beta_{ext}}{\partial b_a} \end{bmatrix} \tag{A9}$$

Once the forward model equations and the Jacobian matrices are constructed, the Gauss Newton optimal estimation framework can be applied in the algorithm to iteratively get the optimal solutions. However, before the iteration, the initial guesses of the PSD parameters need to be calculated first.

Since the PSD parameter α is the least important parameter, the initial guess of α is set to be 1. And then Equations (A5) - (A7) are used to calculate the initial guesses of parameters A and D_g. Considering the terminal fall velocity V_{dq} is retrieved from DM06, the retrieval uncertainty of V_{dq} can be as large as 50%, V_{dq} is not used in the calculation of the initial guess of parameter D_g. Instead, the initial guess of D_g is calculated by Z_e and β_{ext} from Equation (A5) and (A7), and it is written as:

$$D_{gi} = \left[\left(\frac{Z_e}{\beta_{ext}}\right)\left(\frac{2a_a}{a_z}\right)\frac{\Gamma(\alpha + b_a + 1)}{\Gamma(\alpha + b_z + 7)} \right]^{\frac{1}{b_z - b_a + 6}} \tag{A10}$$

And then the initial guess of parameter A is calculated from Equation (A5) as:

$$A_i = \frac{Z_e}{e a_z D_{gi}^{\,b_z+7} \Gamma(\alpha + b_z + 7)} \tag{A11}$$

APPENDIX B

CONVERSION OF AERODYNAMIC DIAMETER

Because aerodynamic diameter D_a is the diameter of an equivalent unit density solid sphere, the total mass of the solid sphere can be expressed as:

$$M(D_a) = \rho_{ice}(\frac{4}{3})\pi(\frac{D_a}{2})^3 \tag{B1}$$

Using the effective ice particle density, the mass can be calculated as:

$$M(D) = \rho_{eff}(D)(\frac{4}{3})\pi(\frac{D}{2})^3 \tag{B2}$$

where ρ_{eff} is the effective ice particle density, which be expressed as:

$$\rho_{eff}(D) = aD^b \tag{B3}$$

Using Equation (B1) and (B2), D can be expressed as:

$$D = (\frac{\rho_{ice}}{a} D_a^{\,3})^{\frac{1}{3+b}} \tag{B4}$$

REFERENCES

Arnott, W.P., Y. Dong, and J. Hallett, 1994: Role of small ice crystals in radiative properties of cirrus: A case study, FIRE II, November 22, 1991. *Journal of Geophysical Research*, **99**, 1371-1381.

Ansman, A., M. Riebesell, and C. Weitkamp, 1990: Measurement of atmospheric aerosol extinction profiles with a Raman lidar. *Optics Letters*, **15**, 746-748.

Aydin, K., and T. M. Walsh, 1999: Millimeter wave scattering from spatial and planar bullet rosettes. *IEEE Transaction on Geoscience and Remote Sensing*, **37**, 1138-1150.

Clothiaux, E. E., K. P. Moran, B. E. Martner, T. P. Ackerman, G. G. Mace, T. Uttal, J. H. Mather, M. A. Miller, and D. J. Rodriguez, 1999: The Atmospheric Radiation Measurement Program cloud radars: Operational modes. *Journal of Atmospheric Oceanic Technology*, **16**, 819-827.

Comstock, J.M., R.F. Lin, D.O. Starr, and P. Yang, 2008: Understanding ice supersaturation, particle growth, and number concentration in cirrus clouds. *Journal of Geophysical Research*, **113**, D23211.

Petty, D., J. Comstock, and D. Tuner, 2006: Cirrus extinction and lidar ratio derived from Raman lidar measurements at the Atmospheric Radiation Measurement Program southern site. *Sixteenth ARM Science Team Meeting Proceedings*, Albuquerque, NM, 1-8.

Deng, M., and G. G. Mace, 2006: Cirrus microphysical properties and air motion statistics using cloud radar Doppler moments: Part I: algorithm description. *Journal of Applied Meteorology and Climatology*, **45**, 1690-1709.

Deng, M., and G. G. Mace, 2008: Cirrus microphysical properties and air motion statistics using cloud radar Doppler moments. Part II: Climatology. *Journal of Applied Meteorology and Climatology*, **47**, 3221-3235.

Donovan, D. P., 2003: Ice-cloud effective particle size parameterizations based on combined lidar, radar reflectivity, and mean Doppler velocity measurements. *Journal of Geophysical Research*, **108**, 4573-4591.

Donovan, D. P., M. Quante, I. Schimme, and A. Macke, 2004: Use of equivalent spheres to model the relation between radar reflectivity and optical extinction of ice cloud particles. *Applied Optics*, **43**, 4929-4940.

Doviak, R. J., and D. S. Zrnic, 1984: *Doppler Radar and Weather Observations*. Academic Press, 458 pp.

Field, P. R., R. Wood, P.R. Brown, P.H. Kaye, E. Hirst, R. Greenaway, and J.A. Smith, 2003: Ice particle Interarrival times measured with a fast FSSP. *Journal of Atmospheric and Oceanic Technology*, **20**, 249-261.

Gayet, J. F., and A. Minikin, 2002: Quantitative measurement of the microphysical and optical properties of cirrus clouds with four different in situ probes: evidence of small ice crystals. *Geophysical Research Letters*, **29**, 2230.

Goldsmith, J., F. H. Blair, S. E. Bisson, and D. Turner, 1998: Turn-key Raman lidar for profiling atmospheric water vapor, clouds, and aerosols. *Applied Optics*, **37**, 4979-4990.

Gossard E. E., and R. G. Strauch, 1994: Measurement of cloud droplet size spectra by Doppler radar. *Journal of Atmospheric Oceanic Technology*, **11**, 712-726.

Heymsfield, A. J., and C.M.R. Platt, 1984: A parameterization of the particle size spectrum of ice clouds in terms of ambient temperature and the ice water content. *Journal of the Atmospheric Sciences*, **41**, 846-855.

Heymsfield, A. J., and J. Iaquinta, 2000: Cirrus crystal terminal velocities. *Journal of the Atmospheric Sciences*, **57**, 916-938.

Heymsfield, A.J., and Coauthors, 2003: A General approach for deriving the properties of cirrus and stratiform ice cloud particles. *Journal of the Atmospheric Sciences*, **59**, 3-29.

Heymsfield, A. J., C. G. Schmitt, A. Bansemer, D. Baumgardner, E. M. Weinstock, J. T. Smith, and D. Sayres, 2004: Effective ice particle densities for cold anvil cirrus. *Geophysical Research Letters*, **31**, 2101.

Heymsfield, A. J., 2007: On measurements of small ice particles in clouds. *Geophysical Research Letters*, **34**, L23812.

Ivanova, D., D.L., Mitchell, A.W. Patrick, and M. Poellot, 2001: A GCM parameterization for bimodal size spectra and ice mass removal rates in midlatitude cirrus clouds. *Atmospheric Research*, **59**, 89-113.

Korolev, A., and G.A. Isaac, 2004: Shattering during sampling by OAPs and HVPS. Part I: snow particles. *Journal of Atmospheric and Oceanic Technology*, **22**, 528-542.

Lawson, R. P., B. Baker, B. Pilson, and Q. Mo, 2006: In situ observations of the microphysical properties of wave, cirrus, and anvil clouds, Part II: Cirrus Clouds. *Journal of the Atmospheric Sciences*, **63**, 3186-3203.

Lewis S., A. Heymsfield, C. Twohy, and M. Poellot, 2001: In situ microphysical

measurements of cirrus properties during ARM 2000 IOP. *Eleventh ARM Science Team Meeting Proceedings, Atlanta, Georgia*, 1-9.

Liu, G.S., 2008: A database of microwave single scattering properties for non-spherical ice particles. *Bulletin of the American Meteorological Society*, **89**, 1563-1570.

Mace, G. G., T.P. Ackerman, E.E. Clothiaux, and B.A. Albrecht, 1997: A study of composite cirrus morphology using data from a 94-GHz radar and correlations with temperature and large-scale vertical motion, *Journal of Geophyscial Research*, **102**, 13581-13593.

Mace, G. G., T. P. Ackerman, P. Minnis, and D. F. Young, 1998: Cirrus layer microphysical properties derived from surface-based millimeter radar and infrared interferometer data. *Journal of Geophysical Research*, **103**, 23207-23216.

Mace G. G., A. J. Heymsfield, and M. R. Poellot, 2002: On retrieving the microphysical properties of cirrus clouds using the moments of the millimeter-wavelength Doppler spectrum. *Journal of Geophysical Research*, **107**, 4815-4841.

Mace, G. G., E. E. Clothiaux, and T. P. Ackerman, 2001: The composite characteristics of cirrus clouds: Bulk properties revealed by one year of continuous cloud radar data. *Journal of Climate*, **14**, 2185-2203.

Matrosov, S. Y., 1997: Variability of microphysical parameters in high-altitude ice clouds: Results of the remote sensing method. *Journal of Applied Meteorology*, **36**, 633-648.

Matrosov, S. Y., and Coauthors, 1998: Comparisons of ice cloud parameters obtained by combined remote sensor retrievals and direct methods. *Journal of Atmospheric and Oceanic Technology*, **15**, 184-196.

Matrosov, S. Y., and A. J. Heymsfield, 2000: Use of Doppler radar to assess ice cloud particle fall velocity-size relations for remote sensing and climate studies, *Journal of Geophysical Research*, **105**, 22427-22436.

Mitchell, D. L., 1996: Use of mass- and area-dimensional power laws for determining precipitation particle terminal velocities. *Journal of the Atmospheric Sciences*, **53**, 1710-1723.

Mitchell, D. L., S.K. Chai, Y. Liu, A.J. Heymsfield, and Y. Dong, 1996: Modeling cirrus clouds. Part I: Treatment of bimodal size spectra and case study analysis. *Journal of the Atmospheric Sciences*, **53**, 2952-2966.

Nelder, J. A. and R. Mead, 1965: A simplex method for function minimization. *Computer Journal*, **7**, 308-313.

Platt, C., and R. Martin, 1997: A parameterization of the visible extinction coefficient of ice clouds in terms of the ice/water content. *Journal of the Atmospheric Sciences*, **54**, 2083-2098.

Protat, A., J. Delanoe, D. Bouniol, A.J. Heymsfield, A. Bansemer, and P. Brown, 2007: Evaluation of ice water content retrievals from cloud radar reflectivity and temperature using a large airborne in situ microphysical database. *Journal of Applied Meteorology and Climatology*, **46**, 557-572.

Roger, C. D., 2000: *Inverse Methods for Atmospheric Sounding: Theory and Practice*. World Scientific, 240 pp.

Stephens, G. L., 2005: Cloud feedback in the climate system: A critical review. *Journal of Climate*, **18**, 237-273.

Turner, D.D., 2004: *Raman Lidar Handbook*, DOE/ARM TR-038, 29 pp.

Twohy, C. H., A.J. Schanot, and W.A. Cooper, 1997: Measurement of condensed water content in liquid and ice clouds using an airborne counterflow virtual impactor. *Journal of Atmospheric and Oceanic Technology*, **14**, 197-202.

Twohy, C. H., J.W. Strapp, and M. Wendisch, 2003: Performance of a counterflow virtual impactor in the NASA icing research tunnel. *Journal of Atmospheric and Oceanic Technology*, **20**, 781-790.

Wang, Z., and K. Sassen, 2001: Cirrus cloud microphysical property retrieval using lidar and radar measurements, part I: Algorithm description and comparison with in situ data. *Journal of Applied Meteorology*, **41**, 218-227.

Wunsch, C., 2006: *Discrete Inverse and State Estimation Problems with Geophysical Fluid Applications*. Cambridge University Press, 384 pp.

Zhdanov, M., 2002: *Geophysical Inverse Theory and Regularization Problems*. Elsevier Science, 633 pp.